Vibration reduction of monopile-supported offshore wind turbines based on finite element structural analysis and active control

Philip Alkhoury, Mourad Aït-Ahmed, Abdul-Hamid Soubra, Valentine Rey

Vibration reduction of monopile-supported offshore wind turbines based on finite element structural analysis and active control

Philip Alkhoury[1], Mourad Aït-Ahmed[1], Abdul-Hamid Soubra[1], Valentine Rey[1]

[1]University of Nantes

Correspondence: Philip Alkhoury, University of Nantes, Saint-Nazaire, France.

Email: philip.alkhoury@etu.univ-nantes.fr

Abstract

A finite element (FE) structural analysis based on a commercial software is combined with an observer-based active control to study the real-time performance of an Active Tuned Mass Damper (ATMD) in reducing the fore-aft vibration of a monopile-supported offshore wind turbine (OWT). Firstly, a reduced order MDOF model was established and used to design a Linear Quadratic Regulator. Secondly, the controller was combined with an observer to minimize the required number of sensors. Thirdly, co-simulations between the high-fidelity FE software and the optimized controller were performed. The aim was to test the robustness of the MDOF model-based controller in terms of OWT vibration reduction when the ATMD is used within a structural FE commercial software. The optimized controller applied to the FE mechanical model of the OWT proved to be efficient, the RMS reduction ratio of the tower top displacement being around 60%. Given the increasing size and capacity of OWTs, the proposed co-simulation technique combining a large deformation structural analysis based on a FE commercial software with an optimized observer-based active control can serve as a tool for the final design stage of the next-generation dynamically-sensitive OWT structures to accurately capture their dynamic responses in the presence of ATMDs.

Keywords: Offshore wind turbine (OWT), Vibration, ATMD, Active controller, LQR control, Finite element analysis.

1. Introduction

Wind energy has received a vast attention in recent years as being one of the most promising renewable energy resources. Considering the high and steady offshore wind speeds, the onshore

space limitation, and the less visual and noise pollution in marine areas, multi-megawatt offshore wind turbines (OWTs) have gained more attraction than their onshore counterparts. However, because of the simultaneous severe action of wind and wave loads found in marine areas, multi-megawatt OWTs suffer from excessive vibrations which may lead to structural fatigue damage, reduction of the design lifetime and an increase of the operational and maintenance cost. It is therefore necessary to mitigate the unwanted vibrations of the OWTs in order to ensure their safe operation. In response to this challenge, structural vibration control, which has been successfully employed in civil engineering structures, became a very active area of research for OWTs (Zuo et al., 2020). The control methods can be mainly divided into three categories namely passive, semi-active and active (Zuo et al., 2020).

Passive control of OWTs makes use of constant parameters and does not require energy to function. Passive control systems have been widely studied in the last decade. Indeed, different passive energy dissipation devices were proposed in literature such as the tuned mass dampers (TMDs) (Murtagh et al., 2008; Lackner and Rotea, 2011a; Zuo et al., 2017; Hussan et al., 2018), the tuned liquid column dampers (TLCDs) (Colwell and Basu, 2009), the three-dimensional (3D) pendulum tuned mass dampers (3D-PTMDs) (Sun and Jahangiri, 2018; Jahangiri and Sun, 2020; Zhu et al., 2021; Jahangiri et al., 2021), the recent inerter-based TMDs (Hu et al., 2018; Zhang and Hoeg, 2021) and many other novel devices (cf. Zuo et al., 2020). In this regard, Murtagh et al. (2008) installed a TMD in the nacelle to reduce the wind-induced vibration of the tower. In their work, a simplified multi-degrees-of-freedom (MDOF) model was used to study the effectiveness of the passive TMD. Lackner and Rotea (2011a) modified the aero-servo elastic code FAST where two independent TMDs were installed in the nacelle to control the fore-aft and side-to-side vibrations. Multiple TMDs (MTMDs) were proposed by Zuo et al. (2017) and Hussan et al. (2018) to mitigate the first and second vibration modes in the presence of seismic loads. Their findings showed the capability of MTMD in mitigating the tower

vibration induced not only by the fundamental vibration mode but also higher modes. Colwell and Basu (2009) examined the usage of a TLCD to reduce the tower excessive vibration and found that implementing a TLCD could prolong the tower lifetime and increase the structural safety. Sun and Jahangiri (2018), Jahangiri and Sun (2020) and Zhu et al. (2021) showed that the 3D-PTMD outperforms traditional linear TMDs in the sense that 3D-PTMD can provide better mitigation of the tower top response under misaligned wind and wave excitations. To enhance the performance of the 3D-PTMD, Jahangiri et al. (2021) proposed a viscoelastic cylindrical pounding layer to increase the dissipation of kinetic energy *via* pounding. Their results showed that the pounding 3D-PTMD is more robust than the dual linear TMDs and regular 3D-PTMD when facing off-tuning issues. Finally, Hu et al. (2018) and Zhang and Hoeg (2021) proposed using an inerter-based TMD to reduce the physical mass of a conventional TMD system while maintaining the same performance. Notice that, although passive control methods can assure the mitigation of OWT vibration to some extent provided that they are properly tuned, they can be easily off-tuned as soon as the natural frequency of the OWT changes, thus resulting in ineffectiveness of the system and even increased vibration (cf. Hemmati and Oterkus, 2018). The natural frequency of the OWT can change mainly due to possible structural damage or even degradation/stiffening of the soil properties (depending on soil type) under the cyclic environmental excitations. These situations may raise concerns regarding the use of passive control systems in OWTs for their whole lifetime, and the use of more advanced vibration control devices needs to be examined.

Compared to passive control systems, semi-active control devices possess time-adjustable parameters tuned based on a feedback signal. Additional sensors, control algorithms and a small amount of energy are required in such systems. Existing literature showed that semi-active TMDs (STMDs) are more effective than passive TMDs in reducing the vibration of linear and nonlinear structures subjected to stationary and non-stationary excitations (Nagarajaiah, 2009).

In this regard, Arrigan et al. (2011) implemented STMDs to control the wind turbine blade flapwise vibration. The authors used a frequency-tracking algorithm for re-tuning the STMD in real-time. Semi-active control was also studied by Sonmez et al. (2016) but for TLCDs where a control algorithm based on short-time Fourier transform (STFT) to track the frequency was used. It should be noted that only the natural frequency was tuned in real time in the previous studies while the damping ratio remained constant. To consider the influence of the damping ratio, Sun and Nagarajaiah (2014) proposed a new control algorithm to tune both the natural frequency and damping ratio of the STMD in real time. The authors observed improved mitigation effect when both the frequency and the damping ratio were tuned. Also, Sun (2018) investigated the use of STMDs for monopile-supported 5 MW NREL OWTs in the presence of environmental loads and post-earthquake damage to soil and tower stiffness. In their work, additional mitigation effect was achieved by employing an advanced short-time Fourier transform (STFT)-based control algorithm where both the damping ratio and the natural frequency of the STMD were re-tuned in real-time. More recently, Sun et al. (2021) introduced a new adaptive tuning algorithm and a schematic tuning system to the previously developed passive 3D-PTMD (Jahangiri and Sun, 2020) to make it a 3D adaptive PTMD (3D-APTMD). The natural frequency as well as the damping property of the 3D-APTMD were tuned in real time to match the wind turbine time-varying dominant frequency caused by environmental and structural property variations. Their results showed that the proposed 3D-APTMD outperforms the dual linear TMDs and 3D-PTMD as it can rapidly and accurately sense the structural property variations.

In addition to semi-active control, active vibration control of wind turbines has been studied in recent years and demonstrated its effectiveness in reducing the excessive vibrations of both tower and blades. In general, active control requires a power source to perform its function. It applies directly an active force to the passive device through a controlled actuator commanded

by predefined suitable algorithms based on sensor measurements of the structural response. In the research works on the active vibration mitigation of OWT tower or blade, the active tuned mass dampers (ATMDs) were most commonly used and different control algorithms were proposed such as H_∞, linear quadratic LQ, static state feedback, etc. The ATMD consists of a passive TMD supplemented by an actuator parallel to the spring and damper. Lackner and Rotea (2011b) implemented an ATMD within the aero-elastic simulator FAST to control the out-of-plane tower vibration of a floating barge-type OWT. A H_∞ loop shaping approach was used to design the ATMD controller. Fatigue load reductions up to 30% or more were achieved compared to a passive TMD case. Fitzgerald et al. (2013) proposed the use of an ATMD and Fitzgerald and Basu (2014) used cable-connected ATMDs (CCATMDs) installed inside the wind turbine blades to reduce the edgewise vibrations. In the two studies, the performance of the ATMD/CCATMD was examined using MDOF models for the wind turbine and an optimal linear quadratic regulator (LQR) controller. Also, the soil-structure interaction (SSI) was completely neglected. Fitzgerald et al. (2018) used an ATMD installed in the nacelle in the flapwise direction to study its effect on the structural reliability of the wind turbine tower for different wind speeds. A MDOF model of the NREL 5 MW wind turbine without considering the SSI was employed and the active force was obtained from a gain-scheduled LQR controller. Their findings showed that the active controller increases the structural reliability of the tower. Fitzgerald and Basu (2016) considered the SSI within a MDOF model of the NREL 5 MW to control the fore-aft wind tower vibration using LQR controlled ATMDs. In their work, a simplified model consisting of two rotational springs at the base of the tower was used to describe the SSI. Their results showed the effectiveness of the ATMD for vibration control in the presence of SSI. It should be noted herein that in all of the aforementioned studies, all the system states were used within the active control scheme assuming that all the measurements are possible. However, in practice this may not be physically feasible. Finally, a review paper

by Rahman et al. (2015) examined the performance of passive and active TMD systems installed in wind turbines. They indicated that the optimal control based on LQR or H_∞ optimization is a preferred approach for the development of active control laws used in ATMD systems.

In almost all of the aforementioned literature concerning the vibration control of OWTs using ATMDs, the effectiveness of ATMDs was studied based on simplified coupled MDOF analytical models for the wind turbine in which the wind turbine components (tower and blades) were merely modeled as flexible elastic beams using the modal coordinates approach and the SSI was either neglected or simply represented by uncoupled springs at the tower base. The modal coordinates approach was then implemented within a standard program for control development such as Matlab/Simulink. The use of such approach is of course a quite suitable choice, particularly in terms of the reduction in the computational burden required to study the structural vibration of the OWT structure. Notice however that MDOF analytical models are unable of properly considering the wind and wave loading distributions along the different OWT components due to the limited number of DOF involved in such models. More importantly, the increasing size and capacity of OWTs renders the OWTs more dynamically-sensitive. Thus, a large deformation FE structural analysis is required to accurately capture their dynamic responses. It should be noted herein, that the consideration of the large deformation of the OWT superstructure and the monopile foundation was found to be of utmost importance while simulating the nonlinear dynamic responses of the OWT under stochastic environmental loads. Indeed, the effect of the consideration of the large deformation of the OWT was studied recently by the authors of this paper (see Alkhoury et al., 2022) where the neglection of the large deformation of the OWT superstructure and monopile foundation resulted in an underestimation of the OWT dynamic responses where the peak and RMS relative differences were found to be respectively 10.3% and 8.4% for the tower top displacement and 14.4% and

12% for the monopile displacement at mudline; simple MDOF models being unable to consider the large deformation of the OWT superstructure and foundation. Finally notice that as monopile-supported OWTs have stringent Serviceability Limit State (SLS) requirements and need to be installed in variable and often complex ground conditions, their foundations and their complex interaction with the soil are challenging and shall be considered with special care during the design phase; MDOF analytical models being uncapable of properly describing the monopile-soil interaction**.** Therefore, the consideration of a more reliable mechanical model that involves (i) a high-fidelity modelling of the OWT based on a large deformation FE analysis and (ii) a suitable modelling of the soil-structure interaction is of paramount importance to accurately capture the dynamic responses of the next-generation dynamically-sensitive OWTs in the presence of TMDs and ATMDs.

In the aforementioned studies that used MDOF models to perform ATMD control on OWTs, the controllers were synthetized based on the assumption that all the system state variables are measurable. However, in practice not all the system state variables can be measured. The reasons are that either this may not be physically feasible or that the sensors required are too expensive. Therefore, the reduction of the required sensors *via* the incorporation of a state-space observer (estimator) is desirable when designing a controller.

In this paper, finite element analysis (FEA) and active control are combined in order to simulate what the real-time ATMD effect would be on the fore-aft vibration of a monopile-supported multi-megawatt OWT installed in sandy soil and subjected to combined wind and wave loads. The DTU 10 MW reference wind turbine (cf. Bak et al., 2013) which is representative of utility-scale multi-megawatt OWTs is considered. In this work, the OWT structural model (including the soil-structure interaction) is developed within the commercial FE code Abaqus, while the controller is synthetized within Matlab/Simulink. A user-defined Fortran subroutine is written to provide a real-time communication (i.e. co-simulation) between Abaqus and the optimal

control algorithm. Abaqus was chosen as the FE software because of its powerful capabilities and its ability to incorporate user-defined Fortran subroutines. Notice that, in the context of literature, FE analysis and active control are classical approaches and thus, the present paper does not bring a new methodology. Furthermore, the use of FE software with control is not new for smart and morphing structures (Ray et al., 2000; Baillargeon and Vel, 2005; Bertagne and Hartl, 2014), but it is certainly new for OWT applications. Indeed, this paper makes use of the 3D FEA-based mechanical model of the 10 MW DTU wind turbine superstructure (monopile, transition piece, tower, blades, hub and nacelle) recently developed by the authors of this paper (see Alkhoury et al., 2021) to which a TMD is now added at the top of the tower in the fore-aft direction. A large deformation FE analysis of the OWT superstructure and the monopile foundation is adopted. The monopile-soil interaction is considered in this paper using the distributed nonlinear soil spring model by Fuentes et al. (2021), which is suitable for large diameter monopiles. The aim of using a distributed soil spring model instead of a 3D soil continuum (as is the case in Alkhoury et al., 2021) is to obtain a sufficiently accurate soil-monopile interaction model with a reduced computational time. The 3D FE model of the OWT is then coupled with an observer-based LQR controller. The aim of the incorporation of the state observer within the active control scheme is to reduce the required number of measurable states as not all system states are measurable in practice. Notice that the controller was designed in this paper based on a reduced order linear time-invariant MDOF model that was derived from an existing MDOF analytical model given by Sun (2018) for a monopile-supported OWT incorporating a TMD. The aim of the reduction is to deliver a simple model that efficiently captures the major vibration characteristics that are of interest in our study. The robustness of the proposed MDOF model-based controller, when combined with a structural FE commercial software, was tested by examining the ATMD performance in mitigating the tower vibration computed with the FE software in the presence of stochastically simulated wind and wave

loading scenarios. It should be emphasized here that the technique presented in this paper is not meant to replace the conventional active control methods (that are based solely on MDOF analytical models) as they are certainly still faster, and in particular more appropriate for the selection and tuning of controller parameters. However, given the increasing size and capacity of OWTs, the presented work could be useful as a final design stage to accurately capture the OWT dynamic system response *via* a rigorous large deformation FE structural analysis.

This paper is organized as follows: a description of the 3D FE mechanical model of the DTU 10 MW reference wind turbine incorporating a TMD is briefly presented in section 2. Section 3 describes the workflow for the implementation of the active control scheme on the 3D FE structural model using a Fortran code. Section 4 investigates the dynamic response of the OWT under three different loading scenarios and in the presence of three different TMD mass ratios. It examines the relevance of the ATMD in the mitigation of the tower top fore-aft vibration using the proposed combined FEA-active control scheme. It also examines (i) the robustness of the reduction of the MDOF model, and (ii) the importance of the incorporation of a system state observer within the control scheme. Finally, some conclusions and practical guidance based on the obtained results are presented in section 5.

2. Mechanical model

2.1 DTU 10 MW reference wind turbine

The OWT system selected in this study is consistent with the reference DTU 10 MW three-bladed OWT defined by Bak et al. (2013). This turbine is representative of multi-megawatt OWTs being manufactured today. It is characterized by a tower height of 115.63 m (a hub height of 119 m) and a decreasing diameter and thickness profile from bottom (8.3 m, 0.038 m) to top (5.5 m, 0.02 m). A monopile foundation of 8.3 m outer diameter and thickness of 9 cm is chosen as a support for the wind turbine. The total monopile length of 80 m is composed of three parts: 45 m are embedded in the seabed; 25 m are in contact with the sea water and the

remaining 10 m (corresponding to the transition piece) are added above the MSL. Notice that the monopile thickness is chosen following the API (2014) recommendation. The relevant dimensions and properties of the offshore wind turbine (DTU 10 MW) are provided in Figure 1a and Table 1.

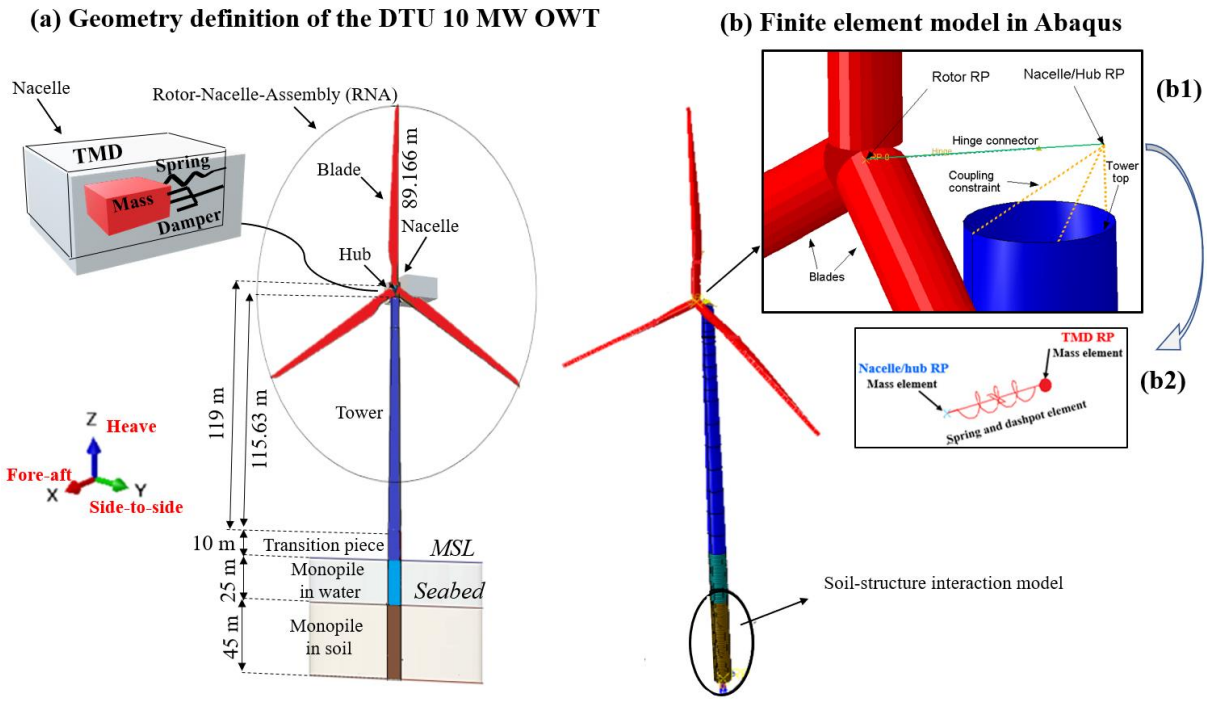

Figure 1: (a) Schematic representation of the DTU 10 MW OWT with a TMD placed in the nacelle in the fore-aft direction; (b) 3D structural FE model in Abaqus of the DTU-10 MW OWT with a TMD placed atop of the tower and considering soil-monopile interaction; (b1) nacelle/hub interconnections with the tower top and rotor; (b2) TMD placed atop of the tower as modeled in Abaqus.

Description	Maximum rated power	10 MW
Blade	Rotor diameter (m)	178.332
	Hub height (m)	119
	Cut-in, rated, cut-out wind speed (m/s)	4 ; 11.4 ; 25
	Cut-in, Rated rotor speed (rpm)	6 ; 9.6
	Length (m)	86.366
	Overall mass (kg)	41,716
Hub-Nacelle	Hub diameter (m)	5.6
	Hub, Nacelle mass (kg)	105520 ; 446036
Tower	Height (m)	115.63
	Mass (kg)	682, 442

Table 1: Properties of the three-bladed upwind DTU 10 MW (Bak et al., 2013).

2.2 Three-dimensional finite element model

2.2.1 Superstructure model

This paper makes use of the 3D structural model of the DTU 10 MW OWT (tower, transition piece, monopile, blades, hub and nacelle) recently developed by the authors of this paper (cf. Alkhoury et al., 2021) making use of the FE code Abaqus/Standard. Only a brief description of the 3D structural model is provided. It should be noted here that the 3D model was developed in Alkhoury et al. (2021) in the aim to compute the natural frequencies of the OWT.

Figure 1b illustrates the whole 3D FE model of the OWT coupled with a TMD, established using Abaqus. In the 3D model, shell elements were used to discretize the steel structure above the MSL (tower and transition piece), while solid elements were used to discretize the steel monopile in order to simulate the soil-monopile interaction. To accurately consider the influence of the blade stiffness and geometry on the OWT dynamic response, each blade was partitioned into 51 segments along its length. A generalized beam cross-section in Abaqus was defined for every segment of the partioned blade and for each cross-section its corresponding mass and stiffness properties were assigned. The nacelle/hub assembly was represented by a lumped mass (point mass in Abaqus) placed at a reference point (RP), whose position is eccentric to the tower top and coincides with the nacelle center of mass. Only the mass and rotary inertia of the assembly were considered at the nacelle/hub RP. A coupling constraint was used to interconnect the nacelle/hub RP with the tower top (Figure 1b) to ensure the transfer of loads from the blades to the turbine structure. In order to simulate the rotation of the blades with respect to the tower, a hinge connector was used between the nacelle/hub RP and that of the rotor (see Figure 1b). It should be noted that the mass and stiffness distribution for the different components (tower, blades, nacelle and hub) of the 3D Abaqus model was validated by comparing the natural frequencies of the 3D model (with fixed tower base, i.e. without transition piece and monopile) with those given in Bak et al. (2013). A very good agreement was observed and more details may be found in Alkhoury et al. (2021).

As the purpose of this study is to investigate the effectiveness of the ATMD in mitigating the OWT tower vibration in the fore-aft direction using the 3D high-fidelity FE model, the TMD was placed within this model inside the nacelle in the fore-aft direction (x-direction in Figure 1). The TMD was modeled as a lumped mass (point mass in Abaqus) placed at a RP and connected to the nacelle/hub RP by a massless spring (spring element in Abaqus) and a viscous dashpot (dashpot element in Abaqus) as shown in Figure 1b. The three rotational and two translational (y-direction and z-direction) degrees of freedom of the TMD RP were completely coupled with those of the nacelle/hub RP. The translational DOF of the TMD RP in the x-direction was kept free in order to simulate its relative displacement with respect to the nacelle in the fore-aft direction.

2.2.2 Model of the soil-monopile system

The soil-structure interaction (SSI) significantly influences the lateral behavior of OWTs. The beam on nonlinear Winkler foundation (called also $p-y$ method) was used in this paper to represent the SSI. This method has been recommended by many design guidelines (see API, 2014; DNV, 2016). Note that a $p-y$ relation is used to obtain the soil reaction p as a function of the pile horizontal displacement y at a given depth. In the $p-y$ method, the monopile is simplified as an elastic beam supported by uncoupled springs with nonlinear behavior representing the lateral soil reaction. The most employed $p-y$ relations are the ones recommended by the American Petroleum Institute (API). However, these relations were originally developed for flexible small-diameter slender piles used in the offshore oil and gas industry and thus lack accuracy when applied to large diameter OWT monopiles with diameters $D \geq 4$ m and aspect ratio (i.e., length-to-diameter L/D ratios) between 4 and 6.

Recently, Fuentes et al. (2021) proposed soil reaction curves for the SSI analysis of large diameter monopiles embedded in cohesionless soils and subjected to lateral loading. The proposed model was calibrated against a number of 3D FE simulations incorporating the

hypoplastic constitutive model for sand (von Wolffersdorff, 1996). In this paper, the distributed nonlinear lateral p - y curves and the nonlinear base shear-displacement curve (called $S_B - y_B$ curve) recently developed by Fuentes et al. (2021), which proved to give satisfactory results with field and centrifuge tests, were adopted to model the SSI (see Figure 2a).

In the present study, a homogeneous deposit of Toyoura clean sand was considered. The corresponding parameters for the hypoplastic model $\{\varphi_c, n_B, e_{d0}, e_{c0}, e_{i0}, \beta\}$ used to derive the soil reaction curves are listed in Table 2 where φ_c is the critical state friction angle, n_B is a parameter which describes the sensitivity of the granular skeleton to changes of pressure, e_{d0}, e_{c0} and e_{i0} are respectively the minimum, the critical and the maximum void ratios calculated for a zero-mean pressure and β represents the change of sand stiffness with the change of the sand relative density. A saturated unit weight of $19.03\,kN/m^3$ and a relative density of 60% were considered for the sand. It should be noted that the model proposed by Fuentes et al. (2021) depends on a certain number of fixed parameters whose values are taken from the parameter identification performed by these authors and which proved to give satisfactory results for large diameter monopiles. Figure 2b shows the $p - y$ curves at different depths ($5 - 45$ m with an increment of 10 m) below the sea bed for the offshore site parameters (Table 2) adopted in this study as obtained using the soil reaction curves proposed by Fuentes et al. (2021). Also Figure 2c shows the $S_B - y_B$ curve at the monopile toe.

Concerning the implementation within Abaqus (i) of the distributed spring model along the monopile and (ii) the spring model at the monopile tip, a 3D representation of the monopile was adopted within this software. The soil was substituted by a set of spring elements. Indeed, 45 equally spaced p - y curves at 1m interval as suggested in Bisoi and Haldar (2014) and as was adopted by Zuo et al. (2018) are placed (in each lateral direction) along the monopile embedded depth (of 45 m) to model the lateral resistance of the soil. Two additional springs were considered at the base of the monopile to simulate the shear at the monopile tip.

It is worth mentioning that although in the present paper a simplified model based on distributed p-y springs was used to represent the SSI, the 3D high-fidelity FE model proposed in this paper is capable of incorporating a 3D soil continuum with an advanced soil constitutive model to simulate the nonlinear behavior of the soil under the stochastic environmental loadings (see Alkhoury et al., 2022).

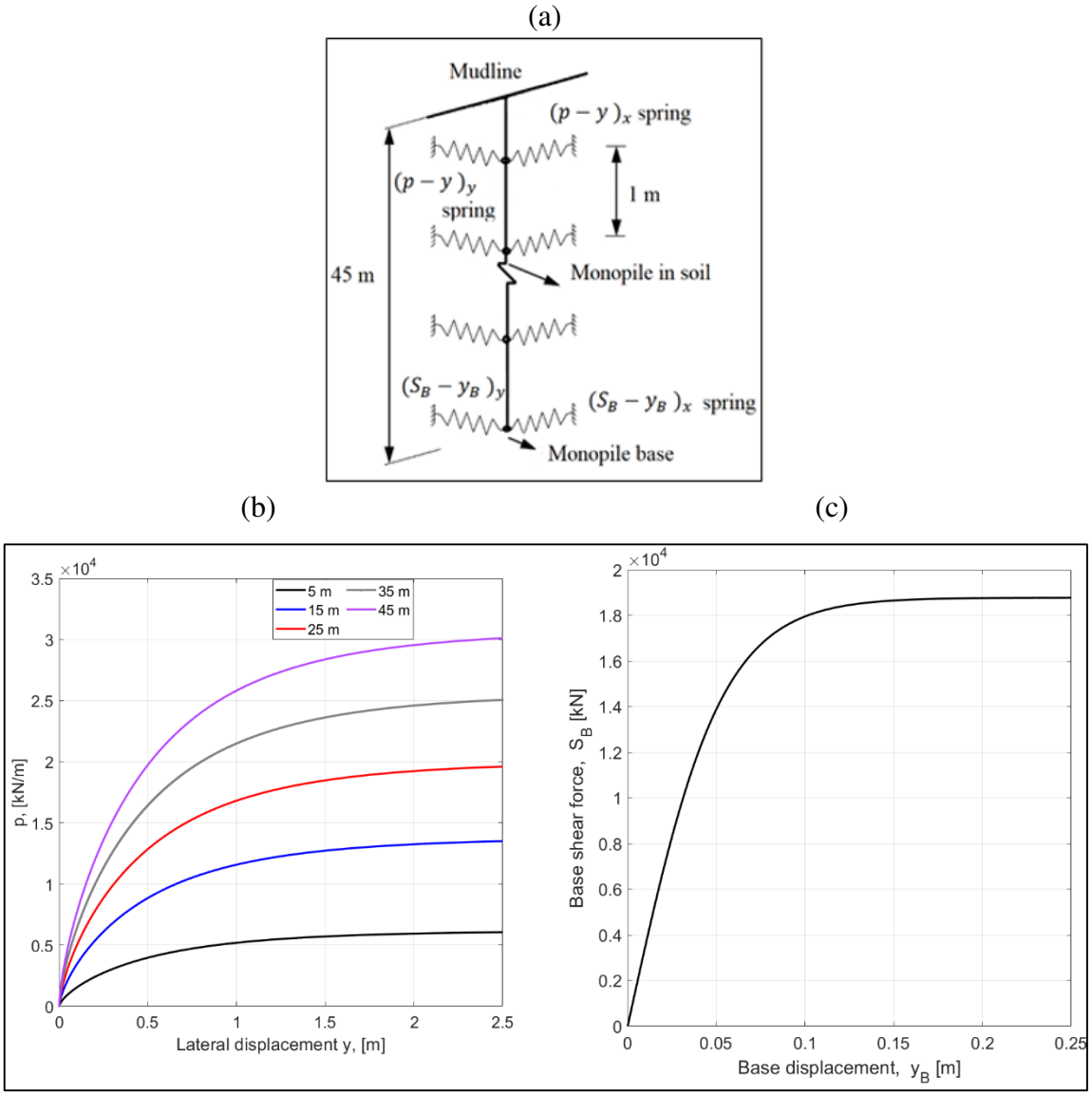

Figure 2: (a) soil-monopile interaction model; (b) and (c) soil reaction curves where (b) represents the distributed $p-y$ curves along the monopile and (c) represents the S_B-y_B curve at the tip of the monopile.

Parameter	φ_c [°]	n_B	e_{d0}	e_{c0}	e_{i0}	β
Value	33	0.27	0.61	0.98	1.10	1.1

Table 2: Parameters of the hypoplastic model for the Toyoura sand (Fuentes et al., 2021).

2.2.3 External loads

The OWT studied in this paper is subjected to combined wind and wave loads. In order to get a realistic representation of a typical offshore site, the wind and wave conditions from the reference project UpWind (see Fischer et al., 2010) were used (see Table 3). This is an offshore site located in the Dutch North Sea, called K13, which is a typical site suitable for monopile foundations in shallow water depths. Load case 6 (LC6), load case 10 (LC10) and load case 17 (LC17) from the K13 site were used in the present study and are presented in Table 3. LC6 and LC10 are characterized by a mean wind speed lying between the cut-in (4 m/s) and cut-out (25 m/s) speed of the 10 MW DTU and representing Design Load Case (DLC) 1.2 Power production from IEC 61400-3 (IEC, 2006), while LC17 (with wind speed above cut-out speed) corresponds to DLC 6.4 Parked (i.e. standing still or idling). The decision behind choosing different DLCs is to check the ATMD effectiveness using the proposed co-simulation technique.

In the present study, the drag wind load acting along the tower, the aerodynamic loads acting along the blades and the hydrodynamic loads acting along the monopile were stochastically simulated from the corresponding Kaimal and Jonswap power spectral density functions respectively as recommended by IEC.

The OWT tower was divided into sixteen segments along its length and the drag force per unit length is assumed to be the same within each segment. The length of each of the seven bottom segments is 11.5 m and that of each of the nine other segments is 5 m. Concerning the blades, each blade was divided into 37 segments and the aerodynamic loads per unit length were assumed to be the same within each segment. The length of each segment corresponds to the data provided in the turbine specifications (cf. Bak et al., 2013). Finally, for the hydrodynamic loads, the monopile in water was divided into ten segments of 2.5 m length each and the hydrodynamic loads were assumed to be constant within each segment. The methods used for

the generation of the different environmental loads used in this paper are detailed in Alkhoury et al. (2022) and are not presented herein for brevity.

Load Case	Mean wind speed at hub height, U_{ref} [m/s]	Turbulence intensity, I [%]	Significant wave height, H_s [m]	Peak spectral period, T_p [m]
6	12	14.6	1.7	5.88
10	20	13.4	2.76	6.99
17	38	11.7	4.9	9.43

Table 3: K13 site characteristic parameters from the UpWind project (Fischer et al., 2010).

2.3 Modal properties

In this section, a structural modal analysis of the OWT in parked condition was carried out in Abaqus/Standard to calculate the vibration frequencies and the corresponding vibration modes in the presence of the soil-monopile interaction adopted in this paper (i.e. the curves presented in Figures 2b and 2c). The obtained natural frequencies were used to model the damping of the OWT in the next subsection. It should be mentioned here that the modal analysis presented in this section makes use of the initial stiffness of the $p - y$ curves. Table 4 provides the computed natural frequencies and the corresponding vibration modes of the DTU 10 MW OWT installed in clean homogeneous Toyoura sand. The results show that the major mode shapes of a monopile-supported OWT are the first bending modes of the tower in the side-to-side and the fore-aft directions. The subsequent modes shapes are those of the blade (Modes 3, 4, 5, 6, 7, 9, 11 and 12) and the second bending modes of the tower (Modes 8 and 10).

Mode	Description	Frequency (Hz)
1	1st Bending tower, side-to-side	0.194
2	1st Bending tower, fore-aft	0.195
3	1st Blade asymmetric, flapwise yaw	0.544
4	1st Blade asymmetric, flapwise tilt	0.589
5	1st Blade collective flap	0.623
6	1st Blade asymmetric, edgewise 1	0.932
7	1st Blade asymmetric, edgewise 2	0.941
8	2nd Bending tower, fore-aft	1.100
9	2nd Blade asymmetric, flapwise Yaw	1.370
10	2nd Bending tower, side-to-side	1.303
11	2nd Blade asymmetric, flapwise tilt	1.701
12	2nd Blade collective flap	1.762

Table 4: Natural frequencies of the monopile-supported 10 MW DTU OWT installed in Toyoura sand as computed by the 3D FE model using the soil reaction curves proposed by Fuentes et al. (2021).

2.4 Damping

Damping is critical to correctly predict the dynamic behavior of an OWT because it is the only factor that limits the amplitude of the response at resonance. In this paper, structural damping, aerodynamic damping, hydrodynamic damping and soil damping are considered (see Bisoi and Haldar, 2014). A structural damping ratio of the blades and tower of 0.43 % and 1 % respectively was considered as given in Bak et al. (2013). An aerodynamic damping of 3.5% was adopted in the fore-aft direction based on Zuo et al. (2018). The hydrodynamic damping caused by the drag between the water and the structure as adopted in this paper is 0.12% following LeBlanc (2009). Concerning the soil damping caused by the energy dissipation due to plastic deformation (Aasen et al., 2017), a constant value of 1% was used in the present study as adopted by Zuo et al. (2018). Summing all components together, the damping ratio in the fore-aft direction for the rotating blades is 3.93% (0.43% for structural damping + 3.5% for aerodynamic damping). For the tower in the presence of SSI, the total damping is 2.12% (1% for structural damping + 0.12% for hydrodynamic damping + 1% for soil damping). The damping of the OWT is modelled in Abaqus by means of material Rayleigh damping (see Chopra, 2012) and the first out-of-plane and in-plane vibration frequencies of the tower and

blades were used to calculate the mass and stiffness coefficients for the tower and blades respectively. The mass and stiffness coefficients are therefore: 0.026 and 0.017 for the tower and 0.172 and 8.59 x 10^{-3} for the blade.

2.5 TMD parameters

In this paper, three different out-of-plane TMD and ATMD mass ratios were considered. The total masses of the TMD and ATMD that were studied were assumed to be respectively $\mu_{TMD} = 1\%$, 2% and 3% of the total wind turbine mass (blades, nacelle/hub, tower, transition piece and monopile in water) which makes about 20,277 kg for $\mu_{TMD} = 1\%$, 40,554 kg for $\mu_{TMD} = 2\%$ and 60,831 kg for $\mu_{TMD} = 3\%$ based on the turbine specifications. Further, the TMDs were tuned to the tower fundamental fore-aft frequency of 0.195 Hz (see Table 4) and three optimum tuning ratios of $\nu_{TMD,opt} = 0.989$, 0.979 and 0.97 for $\mu_{TMD} = 1\%, 2\%$ and 3% respectively were considered using the following empirical expression given by Ghosh and Basu (2007) for lightly damped structures where $\zeta_{tower} = 2.12\%$:

$$\nu_{TMD,opt} = \sqrt{\frac{1-4{\zeta_{tower}}^2-\mu_{TMD}\left(2{\zeta_{tower}}^2-1\right)}{(1+\mu_{TMD})^3}} \quad (1)$$

The optimum TMD damping ratios of $\zeta_{damp,opt} \approx 5\%$, 7% and 8.5% for $\mu_{TMD} = 1\%, 2\%$ and 3% respectively were considered using the following expression derived by Bakre and Jangid (2007):

$$\zeta_{damp,opt} = \sqrt{\frac{\mu_{TMD}\left(1+\frac{3\mu_{TMD}}{4}\right)}{4(1+\mu_{TMD})\left(1+\frac{\mu_{TMD}}{2}\right)}} \quad (2)$$

3 Actively controlled offshore wind turbine model

Active control of the OWT vibration is now investigated where an ATMD is proposed to reduce the tower fore-aft vibrations. Figure 3 shows the general workflow for the implementation of the active control scheme within the 3D FE model in Abaqus. The arrows denote the passage

of control from program to program. The overall structure could be viewed as a combined finite element analysis and active control scheme in time domain, where a robust optimal controller was designed and implemented within a full 3D FE structural model by employing the user-defined Fortran subroutine, UAMP (Abaqus, 2013). UAMP subroutine controls the execution of the control law in a time-dependent manner by generating the necessary control output based on measured sensor values and user-defined solution-dependent state variables predefined in the 3D model. The generated control output is then passed all the way back up the chain into the Abaqus 3D structural model where it is applied to the TMD RP.

The optimal control algorithm was obtained in this work from a reduced order multi-degree-of-freedom (MDOF) analytical model presented in subsection 3.2. The reduced MDOF model was established in this paper making use of an already existing fully coupled MDOF analytical model presented in subsection 3.1. The existing fully coupled MDOF analytical model is the one that was recently developed by Sun (2018) for a monopile-supported OWT incorporating a TMD. For brevity, only the key features of the original and reduced MDOF models are provided herein followed by a detailed description of the active control scheme presented in subsections 3.3 and 3.4.

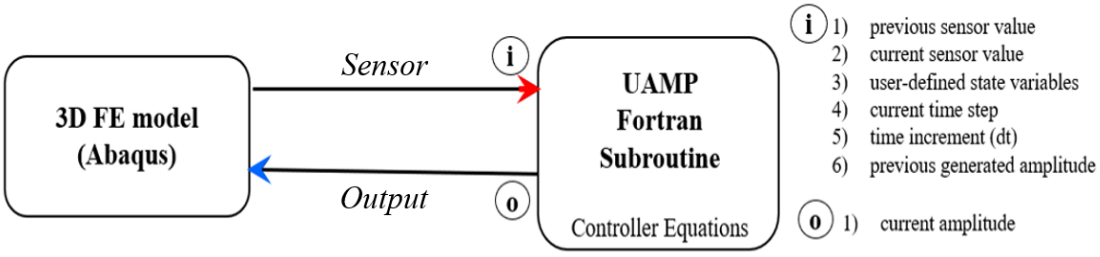

Figure 3: General workflow of the program.

3.1 Overview of the MDOF analytical model by Sun (2018)

In this paper, the fully coupled MDOF analytical model with 11 DOFs as derived by Sun (2018) for a monopile-supported OWT (incorporating a TMD attached to the nacelle in the out-of-plane direction) was employed to obtain the reduced order model of the DTU 10 MW OWT

presented in the next section. Notice that the Equations Of Motion (EOM) were established in Sun (2018) using the Euler-Lagrange formulation. Only the relevant equations are given herein for consistency and the detailed formulation can be found in Sun (2018).

Figures 4a and 4b illustrate the generalized coordinates of (i) the blades in the in-plane and out-of-plane (denoted by $q_1 - q_6$), (ii) the nacelle in the in-plane and out-of-plane (denoted by $q_7 - q_8$) and, (iii) the TMD in the out-of-plane (denoted by q_{11}). The blades were modelled as continuous beams of variable mass and stiffness. In the presented formulation, it has been assumed that the in-plane and out-of-plane displacements at any point r along the blade and at any point z along the tower are given in terms of the fundamental mode shapes and the generalized coordinates q_i. Concerning the soil effect, it was modeled by translational and rotational DOFs (denoted by $q_9 - q_{10}$) at mudline in the fore-aft direction (see Figure 4c). Translational and rotational springs at mudline of constant stiffness coefficients k_x and k_ϕ respectively together with two corresponding dashpots with constant damping coefficients c_x and c_ϕ were used to represent the soil stiffness and damping. For consistency, only the motion of the nacelle to which a TMD with a control scheme is applied will be presented hereafter. The detailed formulation of the blades and tower motion can be found in Sun (2018).

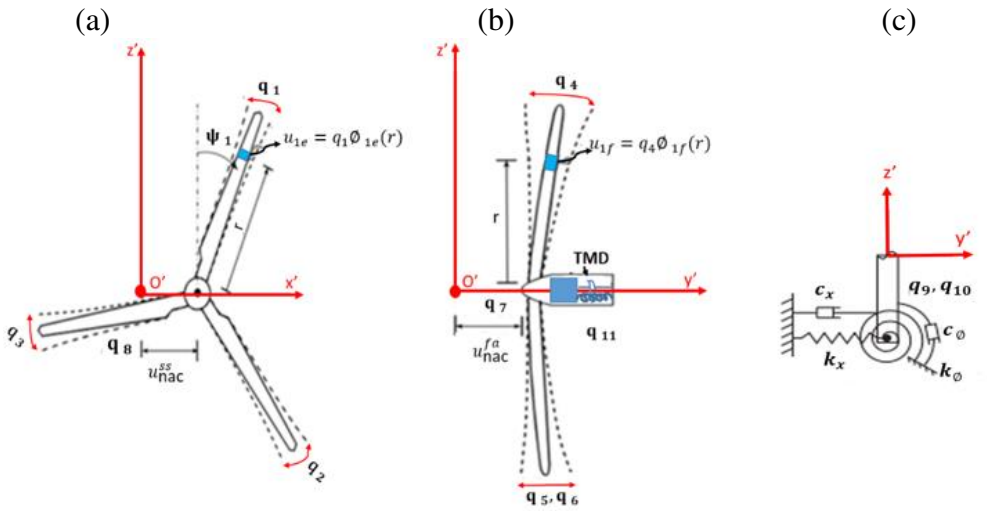

Figure 4: (a) and (b) Generalized coordinates of the turbine blades, nacelle and TMD in the in-plane and out-of-plane respectively and (c) simplified foundation model of the OWT (Modified based on Sun, 2018).

The resultant velocity of the nacelle v_{nac} can be found from the nacelle velocities in both fore-aft and side-to-side directions (v_{nac}^{fa}, v_{nac}^{ss}) as follows:

$$v_{nac} = \sqrt{(v_{nac}^{fa})^2 + (v_{nac}^{ss})^2} \tag{3a}$$

where

$$v_{nac}^{fa} = \dot{q_7} + \dot{q_9} + h\dot{q_{10}} \tag{3b}$$

$$v_{nac}^{ss} = \dot{q_8} \tag{3c}$$

The EOM for the coupled MDOF model of the OWT including the TMD and the foundation as obtained by Sun (2018) are given as follows:

$$[M(t)]\{\ddot{q}\} + [C(t)]\{\dot{q}\} + [K(t)]\{q\} = \{Q_{wnd}\} + \{Q_{wve}\} + \{U_{atve}\} \tag{4}$$

where $[M(t)]_{11\times11}$, $[C(t)]_{11\times11}$, and $[K(t)]_{11\times11}$ are time-dependent mass, damping and stiffness matrices respectively whose details can be found in Sun (2018). $\{Q_{wnd}\}_{11\times1}$ and $\{Q_{wve}\}_{11\times1}$ are the generalized force vectors corresponding to the wind and wave loads and $\{U_{atve}\}_{11\times1} = [\bar{B}]_{11\times1}\{u_{out}\}_{1\times1}$ is the generalized active control force vector; $[\bar{B}]_{11\times1} = \begin{bmatrix} 0_{10\times1} \\ 1 \end{bmatrix}$ being the control influence vector and $\{u_{out}\}_{1\times1}$ the optimal control force to be applied on the actuator connected to the TMD.

It should be noted that the damping of the blades/tower in both directions (edgewise/side-to-side and flapwise/fore-aft) were included in the EOM in the form of stiffness proportional damping as proposed by Fitzgerald and Basu (2016). The damping coefficients of the blade and tower were calculated by using the same damping ratios implemented in the 3D structural model (Section 2.4). The fundamental mode shapes of the blades and tower were computed using BModes (Bir, 2007).

Concerning the soil, the springs stiffness used in the MDOF model (Figure 4c) were calibrated based on the force-displacement curves of the monopile (at mudline) as obtained using the soil-

monopile interaction model used in this paper (i.e. the soil reaction curves presented in Figures 2b and 2c). For each load case (LC6, LC10 and LC17), the peak-values of the resultant lateral load and the overturning moment at the top of the monopile at mudline, were determined and used to perform the calibration as described in Alkhoury et al. (2021). Table 5 gives the peak-values for the three load cases and the corresponding tuned spring stiffness values (taken as the secant stiffness of the force-displacement curves). For the soil damping, the coefficients c_x and c_ϕ were taken equal to $9.34 \times 10^8 \ \ Nms/rad$ with reference to Carswell et al. (2015).

	Peak lateral load at mudline (MN)	Peak overturning moment at mudline (MN.m)	$k_x\ [N/m]$	$k_\phi\ [N.m/rad]$
LC6	1.9	159	1.49×10^9	3.8×10^{11}
LC10	2.35	195	1.40×10^9	3.8×10^{11}
LC17	3.9	221	1.37×10^9	3.6×10^{11}

Table 5: Springs stiffness values of the foundation tuned based on the soil-monopile interaction model proposed by Fuentes et al. (2021) for the three load cases.

3.2 Reduced-order design model

In control system applications, the objective is to obtain a good performance of the closed-loop system. This performance was achieved in this paper by designing a control law based on a suitable model of the system. The model should be simple and must represent the major vibration characteristics of the OWT. For the problem considered in this work, only the first tower modes are of concern since the energy of environmental loads (wind and wave) is mainly concentrated at low frequencies. Moreover, the wind and wave loadings on the tower are larger in the fore-aft direction than in the side-to-side direction. Therefore, the first fore-aft vibration mode of the tower was highlighted in the present work. The tower top fore-aft velocity time history (i.e. ${v_{nac}}^{fa}$ defined in Equation 3b) was chosen as the measurable input parameter for the control algorithm.

In order to increase the effectiveness of the workflow presented in Figure 3, a fourth-order reduced model was identified in this paper and used to define the active control force vector

$\{U_{atve}\}$ as a function of the measured input ${v_{nac}}^{fa}$. The fourth-order reduced model which contains only the four degrees of freedom q_7, q_9, q_{10} and q_{11} was established from the reference model (with 11 degrees of freedom as described above) by applying an appropriate reduction matrix $[R_{Red}]$. It should be noted that the fourth-order reduced model was obtained by omitting the six generalized coordinates of the blades in the flapwise and edgewise directions ($q_1 - q_6$) and the generalized coordinate of the nacelle in the side-to-side direction (q_8). These seven DOFs ($q_1 - q_6$ and q_8) were excluded from the MDOF model because of their negligible inertial effect on the nacelle fore-aft vibration compared to that of the nacelle and the tower DOFs in the fore-aft direction. The state-space representation of order 8 of the reduced-order model (including both the generalized coordinates and their derivatives) is given as follows:

$$\begin{cases} \{\dot{\overline{q_r}}\}_{8\times1} = [R_{Red}][A][R_{Red}]^T\{\overline{q_r}\} + [R_{Red}][B]\{u_{out}\} + [R_{Red}]\left\{\{\overline{Q_{wnd}}\} + \{\overline{Q_{wve}}\}\right\} \\ \{\mathrm{y}\}_{1\times1} = [C][R_{Red}]^T\{\overline{q_r}\} \end{cases} \quad (5)$$

where $\{\overline{q_r}\}_{8\times1} = \begin{Bmatrix}\{q_r\}\\ \{\dot{q_r}\}\end{Bmatrix}$, $\{q_r\}_{4\times1} = \begin{Bmatrix} q_7 \\ q_9 \\ q_{10} \\ q_{11} \end{Bmatrix}$, $[A]_{22\times22} = \begin{bmatrix} 0_{11\times11} & \mathrm{I}_{11\times11} \\ -M^{-1}K & -M^{-1}C \end{bmatrix}$,

$[B]_{22\times1} = \begin{Bmatrix} 0_{11\times1} \\ -M^{-1}[\bar{B}] \end{Bmatrix}$, $[\bar{B}]_{11\times1} = \begin{bmatrix} 0_{10\times1} \\ 1 \end{bmatrix}$, $\{\overline{Q_{wnd}}\}_{22\times1} = \begin{Bmatrix} 0_{11\times1} \\ -M^{-1}Q_{wind} \end{Bmatrix}$,

$\{\overline{Q_{wav}}\}_{22\times1} = \begin{Bmatrix} 0_{11\times1} \\ -M^{-1}Q_{wave} \end{Bmatrix}$, $[C]_{1\times22} = [0_{1\times17} \quad 1 \quad 0 \quad 1 \quad h \quad 0]$

$$[R_{Red}]_{8\times22} = \begin{bmatrix} 0_{1x6} & 1 & 0 & 0 & 0 & 0 & 0_{1x6} & 0 & 0 & 0 & 0 & 0 \\ 0_{1x6} & 0 & 0 & 1 & 0 & 0 & 0_{1x6} & 0 & 0 & 0 & 0 & 0 \\ 0_{1x6} & 0 & 0 & 0 & 1 & 0 & 0_{1x6} & 0 & 0 & 0 & 0 & 0 \\ 0_{1x6} & 0 & 0 & 0 & 0 & 1 & 0_{1x6} & 0 & 0 & 0 & 0 & 0 \\ 0_{1x6} & 0 & 0 & 0 & 0 & 0 & 0_{1x6} & 1 & 0 & 0 & 0 & 0 \\ 0_{1x6} & 0 & 0 & 0 & 0 & 0 & 0_{1x6} & 0 & 0 & 1 & 0 & 0 \\ 0_{1x6} & 0 & 0 & 0 & 0 & 0 & 0_{1x6} & 0 & 0 & 0 & 1 & 0 \\ 0_{1x6} & 0 & 0 & 0 & 0 & 0 & 0_{1x6} & 0 & 0 & 0 & 0 & 1 \end{bmatrix},$$

$\{\mathrm{y}\}_{1\times1}$ being the output of the system to be controlled (i.e. ${v_{nac}}^{fa}$ in Equation 3b) and $\{u_{out}\}_{1\times1}$ is the control force to be applied on the actuator connected to the TMD.

Figure 5 shows a comparison between the Bode plot for the output {y} as given by the reference model by Sun (2018) and the reduced-order model. From this figure, it may be seen that the

frequency-domain of the desired output {y} is defined accurately using the established reduced-order model. Also, the output peak frequency obtained using the MDOF model ($1.23\,rad/s$) agrees well with that obtained from the modal analysis performed on the 3D model (i.e. $2\pi \times 0.195 = 1.225\,rad/s$ as may be seen from Table 4).

Finally, it should be emphasized herein that the established reduced order model (Equation 5) was found to be time-invariant compared to the reference model where $[M(t)]$, $[C(t)]$ and $[K(t)]$ were time-dependent. This time-independency of the reduced order model is due to the fact that the terms omitted are time-dependent and the remaining terms related to the 4 DOFs (q_7, q_9, q_{10} and q_{11}) are time-independent. This time-independency facilitates the implementation of the proposed framework within Fortran and decreases the computational time, as Fortran is not a well-established language for control algorithms compared to standard programs such as MATLAB/Simulink. It is worth noting that Oveisi et al. (2018) have recently presented an attractive interface for establishing a real-time connection between a FE software (such as Abaqus) and Matlab using a Fortran interface which may be used in case of time-variant models.

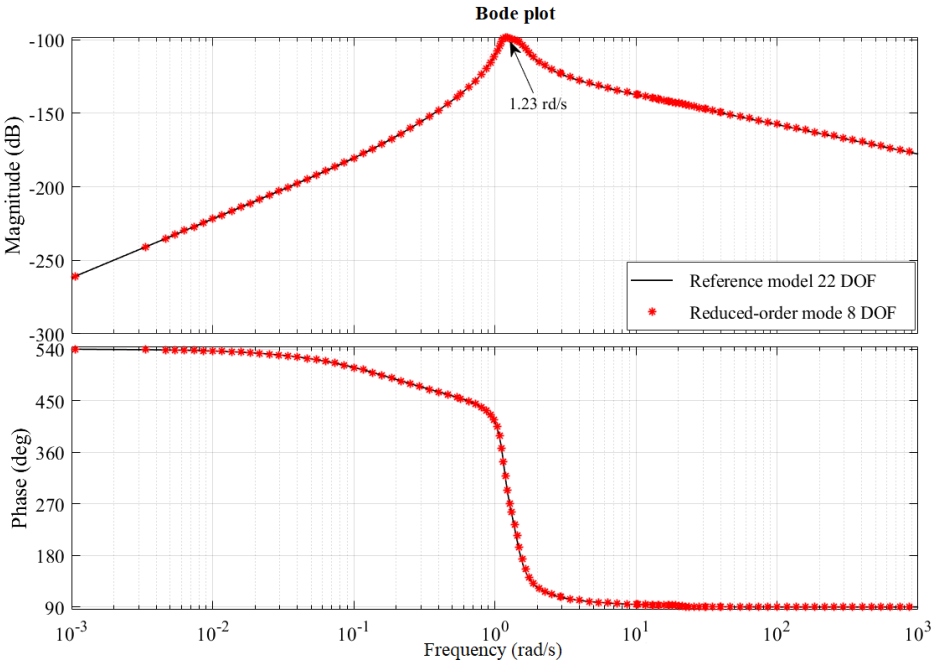

Figure 5: Bode plots of the reference and reduced-order models.

3.3 Observer-based LQR controller

The equations of motion of the fourth-order reduced MDOF model presented above (Equation 5) were used to establish an optimal active control scheme that is able to deliver an appropriate control force on the actuator, i.e. $\{u_{out}\}_{1\times1}$ based on the measured tower top fore-aft velocity time history (output sensor from the 3D FE model in Abaqus). A Linear Quadratic Regulator (LQR) feedback controller was implemented to obtain the required active control force. Notice that an LQR is a popular tool implemented to operate a dynamic system at a minimum cost (Kwakernaak and Sivan, 1972). The linear state LQR feedback is given by:

$$\{u_{out}\} = \left[G_{LQR}\right]\{\overline{q_r}\}_{8\times1} \tag{6}$$

where $\left[G_{LQR}\right]_{1\times8}$ is the LQR feedback gain and $\{\overline{q_r}\}_{8\times1}$ is the reduced-order state vector. The optimal value for $\left[G_{LQR}\right]$ was found by minimizing the following cost function:

$$J_1 = \int_{t_0}^{t_f}[\{\overline{q_r}\}^T[Q]\{\overline{q_r}\} + \{U_{atve}\}^T[R]\{U_{atve}\}]dt \tag{7}$$

Notice that the LQR design assumes that all of the eight state variables $\{\overline{q_r}\}$ in Equation 6 are available for feedback. However; in practice, not all the state variables are measured. The reasons are that either this may not be physically feasible or that the sensors required are too expensive. In this paper, we propose an optimal control scheme which makes use not only of the LQR feedback controller (defined above) but also of a Linear Quadratic (LQ) state observer (estimator). The active control force is thus calculated based on an optimal control scheme which makes use of the robust Linear Quadratic Regulator (LQR) feedback controller combined with a Linear Quadratic state observer.

Figure 6 shows the block diagram of the controlled system with the combined controller–observer used in this work. The LQ observer aims to reconstruct the complete state space information based only on the measured output {y}, knowing the system description (i.e. $[A]$, $[B]$ and $[C]$). The motivation behind the observer development is to provide the regulator an

estimation $\{\widehat{\overline{q_r}}\}$ of the true reduced state vector $\{\overline{q_r}\}$ (Figure 6). Consequently, Eqs. (6) and (7) should be modified by replacing $\{\overline{q_r}\}$ with $\{\widehat{\overline{q_r}}\}$.

The state-space representation of the observer is given as follows:

$$\begin{cases}\left\{\dot{\widehat{\overline{q_r}}}\right\} = [R_{Red}][A][R_{Red}]^T\{\widehat{\overline{q_r}}\} + [R_{Red}][B]\{u_{out}\} + [L]\{\mathrm{y} - \hat{y}\} \\ \{\hat{y}\} = [C][R_{Red}]^T\{\widehat{\overline{q_r}}\}\end{cases} \quad (8)$$

where $\hat{y}$ is the observer estimated output and $[L]$ is the observer gain. $[L]$ was determined in such a way to minimize the observer estimation error $\{\tilde{q}\} = \{\overline{q_r} - \widehat{\overline{q_r}}\}$. The cost function J_2 which has to be minimized for an optimal LQ observer is given as follows:

$$J_2 = \int_{t_0}^{t_f}[\{\tilde{q}\}^T[Q_e]\{\tilde{q}\} + \{\tilde{y}\}^T[R_e]\{\tilde{y}\}]dt \qquad \text{where } \tilde{y} = \{\mathrm{y} - \hat{y}\} \quad (9)$$

In Eqs. (7) and (9), $[Q]$, $[R]$, $[Q_e]$ and $[R_e]$ are weighting matrices used to put emphasize respectively on the system states vector $\{\overline{q_r}\}$, the active control force vector $\{U_{atve}\}$, the estimation error vector $\{\tilde{q}\}$ and the estimated output error vector $\tilde{y}$. Appropriate choice of the LQR weighting matrices ($[Q]$, $[R]$) is crucial when performing LQR control in order to master the dynamics of the system states by using a minimum amount of energy. In this study, the weight $[Q]$ has been set to the identity matrix (i.e. $[Q] = [I]_{8\times8}$), thus assigning the same relative importance to the regulation of each state variable. The weight $[R]$ on the control force was assumed in the form $[R] = \beta$ where β is a scalar. For the ATMD simulations, a sensitivity analysis was carried out in MATLAB and different controllers have been created by varying β. A value of $\beta = 10^{-8}$ was found to ensure a good response reduction with acceptable control effort. The same weighting matrices, $[Q_e] = [I]_{8\times8}$ and $[R_e] = 10^{-8}$ were also found appropriate for the observer to ensure a minimum estimation error $\{\tilde{q}\}$.

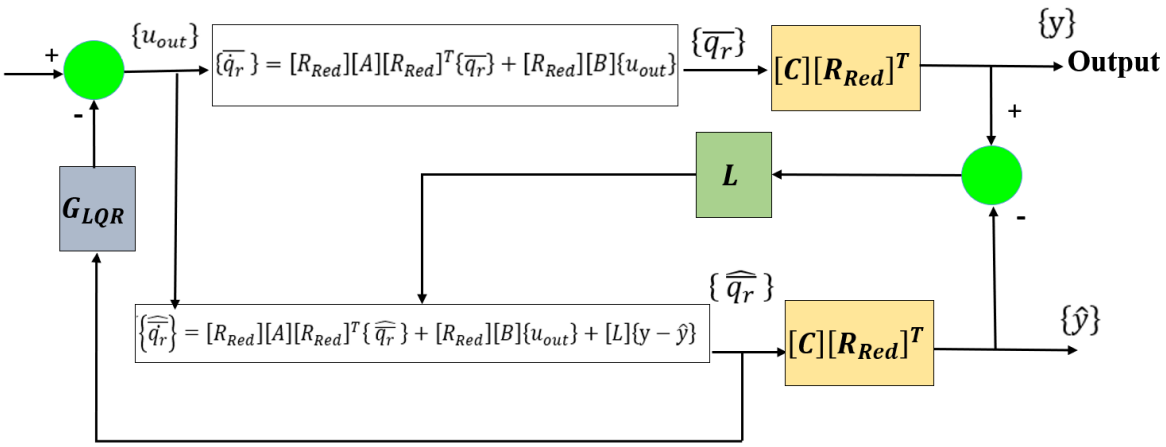

Figure 6: Block diagram of the controlled system.

3.4 Co-simulation between the high-fidelity FE software and the optimized controller

Figure 7 shows a schematic representation (block diagram) of the co-simulation technique used for the vibration mitigation of the OWT tower top. It shows on the left-hand side the Abaqus 3D FE model of the OWT together with the TMD and the active control force. The active control force is calculated and delivered back to the 3D FE model at each time step by an optimized controller coded in a UAMP subroutine (shown in the right-hand side of Figure 7). Indeed, after the determination of the different weighting matrices and as the system state matrices of the reduced-order model ($[R_{Red}][A][R_{Red}]^T$ and $[R_{Red}][B]$) are time-independent, the first order differential equation (Equation 8) was solved within the Fortran subroutine UAMP (see the right-hand block of Figure 7) using the forward Euler numerical integration with fixed small time steps (0.01 s) for the entire duration of the simulation. This method uses the knowledge of the current reduced state space vector $\{\widehat{\dot{q_r}}\}_n$ and its derivative as well as the time step (Δt) to approximate $\{\widehat{\dot{q_r}}\}_{n+1}$. Eight user-defined state variables were assigned within the Fortran subroutine to store the current $\{\widehat{\dot{q_r}}\}_n$ needed for the next time step. Once the observed reduced state vector is obtained, it was multiplied by the LQR feedback gain $[G_{LQR}]$ (see the right-hand block of Figure 7) to provide the active control force to be applied to the TMD in the 3D FE model within Abaqus at each time step (see the left-hand block of Figure 7). For the dynamic analysis in Abaqus, a direct integration scheme with a fixed time step (0.01

s) equal to that used within Fortran was chosen. The step size was chosen small enough to achieve stability of the numerical scheme in each time step and especially during the initial transient response.

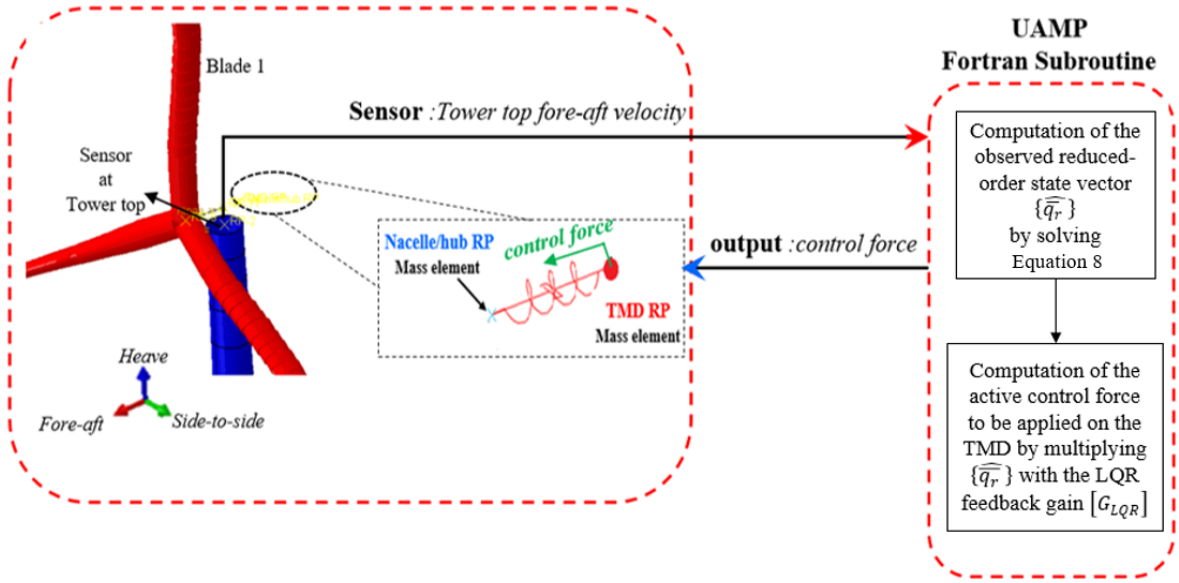

Figure 7: Block diagram for the ATMD.

4 Numerical results

This section is devoted to present the numerical results in the aim of reflecting the two main contributions of this paper which are (i) the implementation of a co-simulation technique to study the real-time performance of an ATMD installed at the OWT tower top in the fore-aft direction making use of the 3D high-fidelity large deformation FE model for the OWT and the optimized controller synthetized based on a reduced-order MDOF model and (ii) the relevance of using the state estimator (observer) within the control law based on the measurement of only the tower top fore-aft velocity.

This section includes three subsections. The first subsection (subsection 4.1) presents the dynamic responses of the OWT obtained in the absence of a TMD and an ATMD. The second subsection (subsection 4.2) gives the dynamic responses of the OWT obtained in the presence of the ATMD and evaluates the practical performance of the ATMD based on the proposed co-simulation technique. Finally, the third subsection (subsection 4.3) studies the relevance of the

incorporation of a state observer (estimator) within the active control. It also examines the significance of the proposed reduction of the DOF in the MDOF model. It should be noted that all the results presented in this section were conducted by employing the FE software ABAQUS/Standard V6.14. The Hilber-Hughes-Taylor (HHT) (Smith, 2015) implicit integrator was used to solve the dynamic equations with a fixed time step $\Delta t = 0.01 s$. The large deformation FE analysis was adopted in the computations. 10-minute simulations for the different load cases (LC6, LC10 and LC17) were run as recommended in IEC 61400-3. This is because the wind turbine design loads are often obtained for the 10-minutes wind speed (Table 3).

4.1 Response of the wind turbine in the absence of the TMD and ATMD

For conciseness and due to space limitation, the blade edgewise and flapwise displacement time histories were not illustrated and only the maximum responses at the top of the tower were presented and discussed in the present study.

Figures 8a and 8b show the displacement time histories at the top of the tower in the fore-aft and side-to-side directions respectively. The black curves are the results for LC17, the red curves are the results for LC10, and the blue curves are those for LC6. As shown in Figure 8a, the maximum fore-aft displacement at the top of the tower is quite large (up to -3.68 m for LC17, -2.91 m for LC10 and -1.88 m for LC6). For the side-to-side displacement at the top of the tower (Figure 8b), the absolute maximum values are 0.53 m for LC17, 0.36 m for LC10 and 0.30 m for LC6. Comparing Figure 8a with Figure 8b, it is obvious that the side-to-side displacements of the tower are much smaller than those in the fore-aft direction for the different load cases. This observation is in conformity with the results obtained by Zuo et al. (2018).

Figure 9 shows the PSDs of the displacement response at the top of the tower in the fore-aft and side-to-side directions for LC17, LC10 and LC6. As shown in Figure 9a, an obvious peak appears at 0.1936 Hz for LC17 and at 0.1945 Hz for both LC10 and LC6. This corresponds to

the first vibration mode of the tower in the fore-aft direction. This means that the first vibration mode is excited by the simulated external loads. For the PSDs in the side-to-side direction, Figure 9b shows a peak at 0.1934 Hz which corresponds to the first vibration mode of the tower in the side-to-side direction. Comparing the results in Figure 9b with those in Figure 9a, it is obvious that the energies are much smaller in the side-to-side direction which results in the smaller tower vibrations in this direction as may be seen from Figure 8. To conclude, the significant structural displacement occurring in the fore-aft direction jeopardizes the performance and safety of multi-megawatt OWTs. Therefore, effective vibration control measures are desirable in the fore-aft direction.

(a) Fore-aft (b) Side-to-side

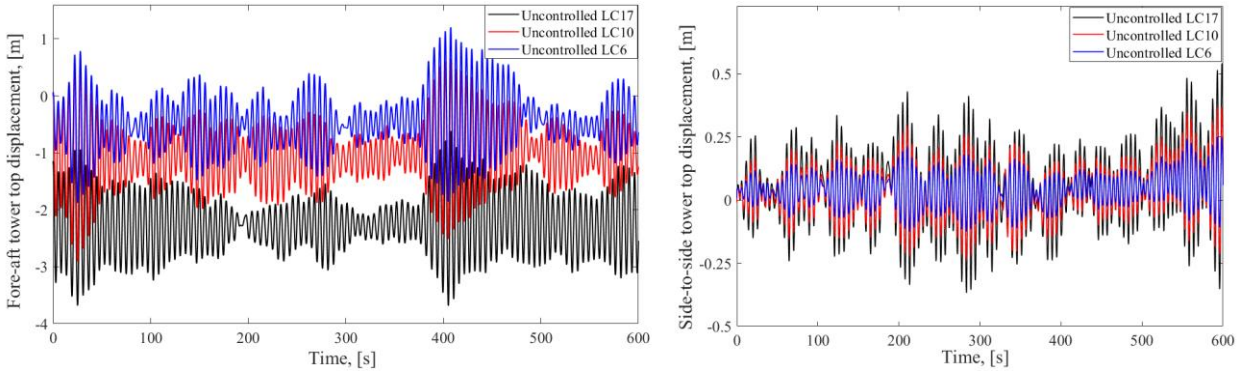

Figure 8: (a) Fore-aft and (b) side-to-side displacement time histories at the tower top for LC6, LC10 and LC17.

(a) Fore-aft (b) Side-to-side

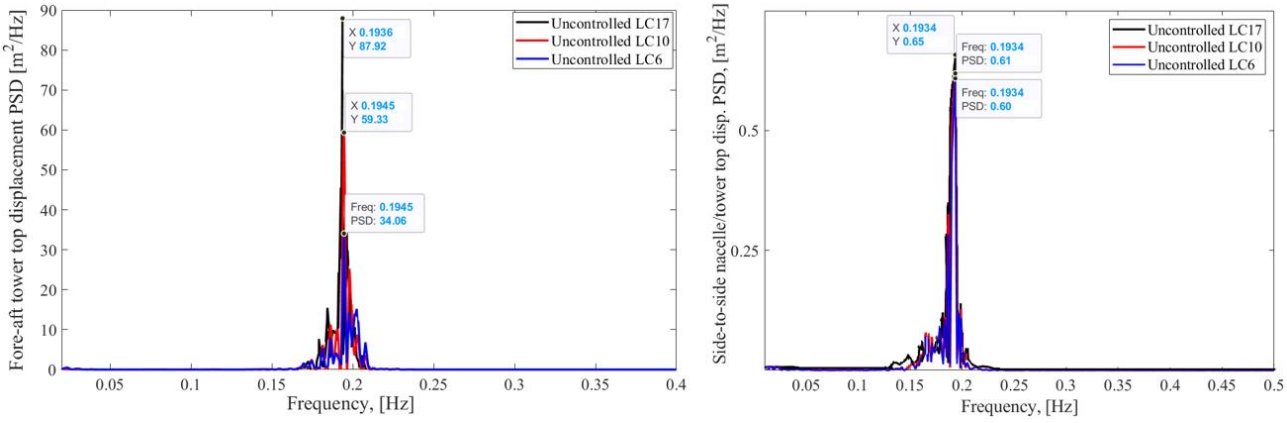

Figure 9: Frequency response of (a) the fore-aft and (b) the side-to-side displacements at the tower top for LC6, LC10 and LC17.

4.2 Response of the controlled wind turbine

This section aims at evaluating the performance of the ATMD in the vibration reduction as obtained using the co-simulation technique proposed in this paper. First, the passive control strategy was investigated by comparing the OWT response in the presence of a passive TMD with that in the absence of TMD (called uncontrolled). Then, the effectiveness of the proposed active control strategy based on an ATMD coupled to the 3D high-fidelity FE model was evaluated by comparing its results with those of a passive TMD coupled to the same 3D high-fidelity FE model. A representative TMD with a mass ratio of 1% was considered with the properties given in section 2.5. Note that the proposed TMD mass (20,277 kg) is around 3 % of the total Rotor Nacelle Assembly (RNA) mass (676,704 kg).

To quantitatively evaluate the mitigation effect of the TMD and ATMD, the peak and root mean square (RMS) reduction ratios of the tower top were calculated as follows:

$$R_{peak\_TMD} = \frac{{U_{un}}^{Peak} - {U_{TMD}}^{Peak}}{{U_{un}}^{Peak}} \quad (10a)$$

$$R_{peak\_ATMD} = \frac{{U_{un}}^{Peak} - {U_{ATMD}}^{Peak}}{{U_{un}}^{Peak}} \quad (10b)$$

$$R_{RMS\_TMD} = \frac{{U_{un}}^{RMS} - {U_{TMD}}^{RMS}}{{U_{un}}^{RMS}} \quad (10c)$$

$$R_{RMS\_ATMD} = \frac{{U_{un}}^{RMS} - {U_{ATMD}}^{RMS}}{{U_{un}}^{RMS}} \quad (10d)$$

where the R_{peak_TMD} and R_{peak_ATMD} (respectively R_{RMS_TMD} and R_{RMS_ATMD}) are the peak response reduction ratios (respectively the RMS response reduction ratios) of the OWT, compared to the uncontrolled case, as obtained in the presence of a TMD (passive control) and an ATMD (active control) respectively. Notice that (${U_{TMD}}^{Peak}$, ${U_{ATMD}}^{Peak}$, ${U_{un}}^{Peak}$) and (${U_{TMD}}^{RMS}$, ${U_{ATMD}}^{RMS}$ and ${U_{un}}^{RMS}$) are respectively the tower top peak and RMS displacements of the OWT (i) in the presence of a TMD, (ii) in the presence of an ATMD and (iii) in the uncontrolled case.

Figures 10a, 11a and 12a illustrate the fore-aft displacement time histories atop of the tower with and without the passive TMD for LC6, LC10 and LC17 respectively and Figures 10b, 11b

and 12b give the corresponding PSDs. From Figures 10a, 11a and 12a, one may observe that the vibration of the tower top was reduced when the passive TMD is used. The peak and RMS reduction ratios (R_{peak_TMD} and R_{RMS_TMD}) were respectively equal to 22.5% and 33.2% for LC6, 28.5% and 38.9% for LC10 and 16% and 19% for LC17. Also, Figures 10b, 11b and 12b show that the response spectrum peak in the case of the TMD was mitigated by 52.4% for LC6, 69% for LC10 and 37% for LC17. It should be noted herein, that the TMD loses its performance at the higher load case (i.e. LC17). This can be explained by the fact that the TMD becomes off-tuned (0.1936 Hz, see Figure 12d) as it was initially calibrated on the first natural frequency of the tower in the fore-aft direction which was equal to 0.1945 Hz.

Figures 10c, 11c and 12c and Figures 10d, 11d and 12d show respectively the time history and the power spectrum of the tower top displacement as controlled by the passive TMD and the ATMD under LC6 (Figure 10), LC10 (Figure 11) and LC17 (Figure 12). From these figures, it is obvious that for all load cases, the tower top vibration was dramatically reduced when an ATMD is used instead of a passive TMD. The peak and RMS reduction ratios (R_{peak_ATMD} and R_{RMS_ATMD}) of the tower top in the case of the ATMD were found to be respectively 45.6% and 59.2% for LC6, 36.2% and 61.3% for LC10 and 29.1% and 51% for LC17. Also, the response spectrum peak was dramatically mitigated when using an ATMD instead of a TMD. Notice herein that the ATMD proved to maintain its performance in terms of the vibration reduction even at the higher load case (i.e. LC17) when compared to the passive TMD which became off-tuned.

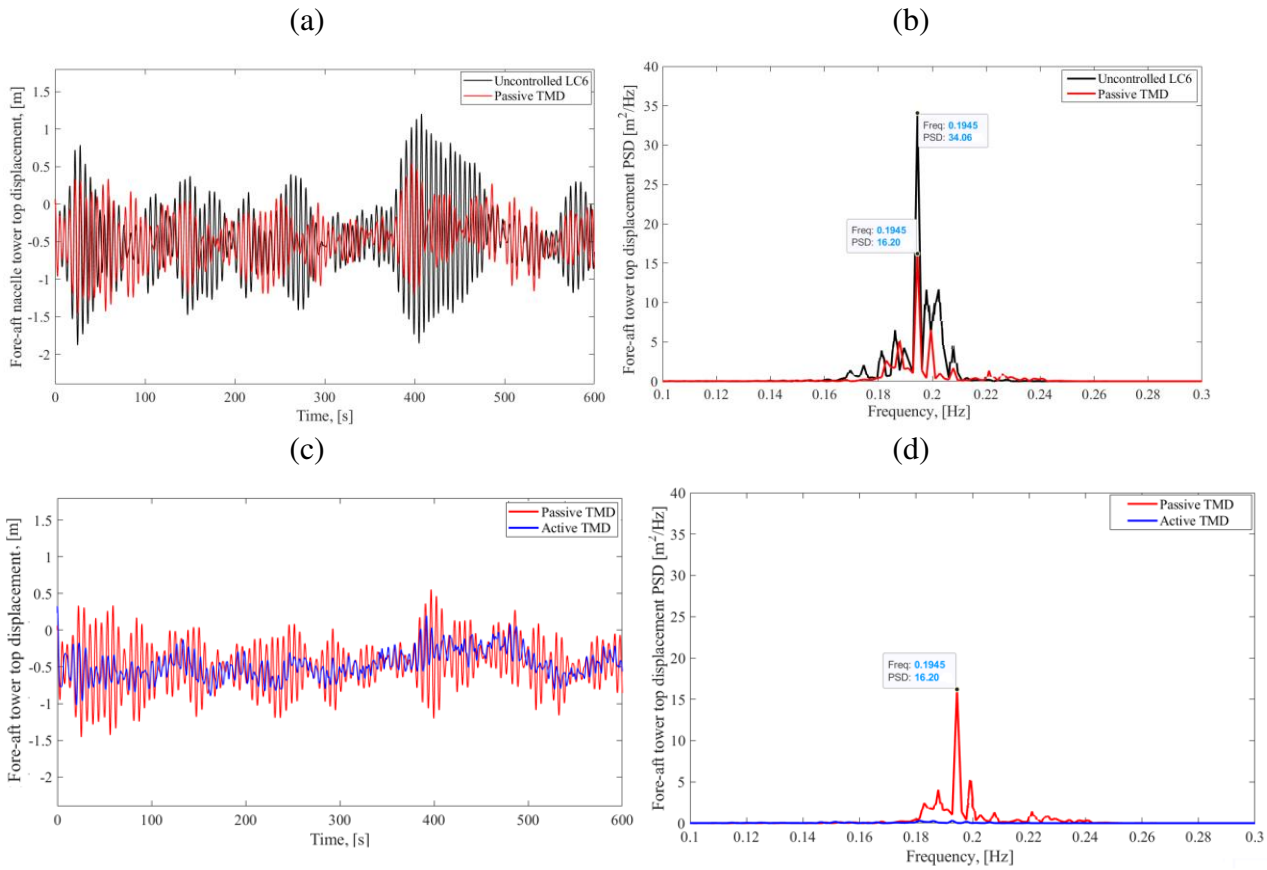

Figure 10: Fore-aft tower top displacement under LC6. (a), (c) Time-history and (b), (d) response spectrum.

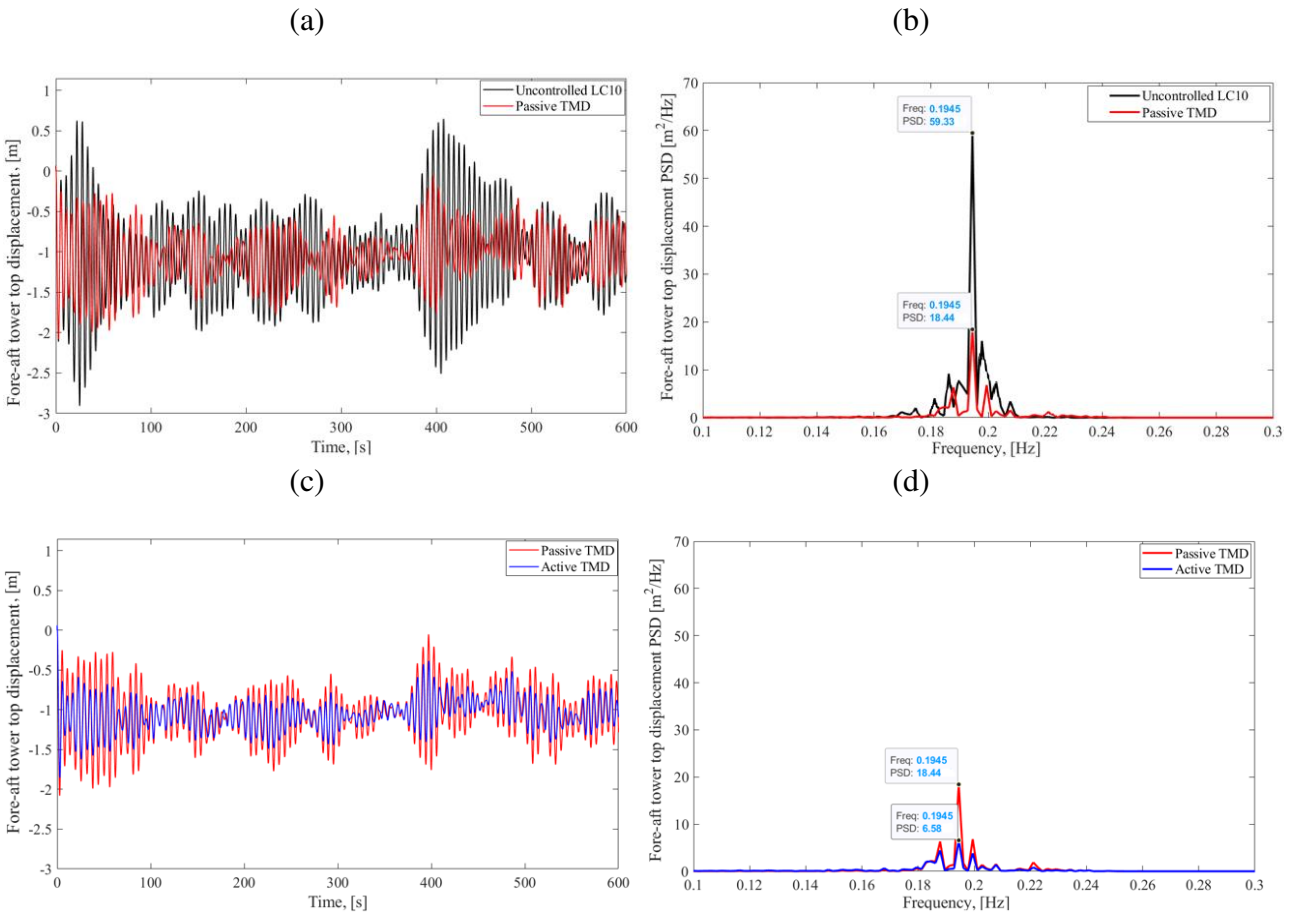

Figure 11: Fore-aft tower top displacement under LC10. (a), (c) Time-history and (b), (d) response spectrum.

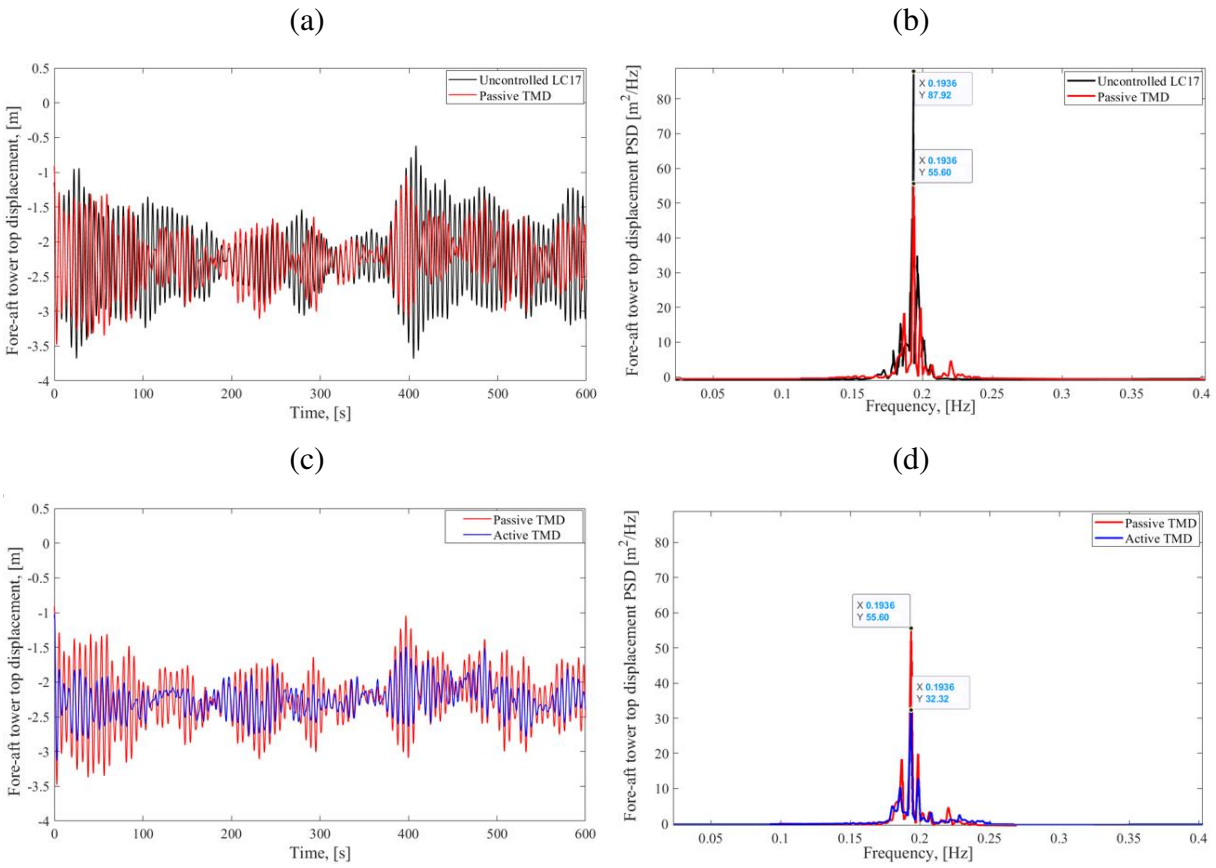

Figure 12: Fore-aft tower top displacement under LC17. (a), (c) Time-history and (b), (d) response spectrum.

In addition to the control of the displacement at the tower top, the TMD and ATMD can provide effective mitigation to the foundation movement at mudline. Figures 13 and 14 illustrate respectively the foundation fore-aft displacement and out-of-plane rotation time histories at mudline in the presence and in the absence of a TMD or an ATMD under LC6 and LC10. It should be noted that a similar reduction was obtained for the foundation responses under LC17 and the results are not presented herein for conciseness. From Figures 13 and 14, one may observe that the use of passive or active TMD decreases both the fore-aft displacement and the rotation of the foundation at mudline. The active control resulted in increased displacement and rotation reduction at mudline. This reduction will help in mitigating the fatigue loads applied to the foundation, which results in prolonging the service lifetime of the OWT and reducing its potential maintenance cost.

(a) Load case 6 (b) Load case 10

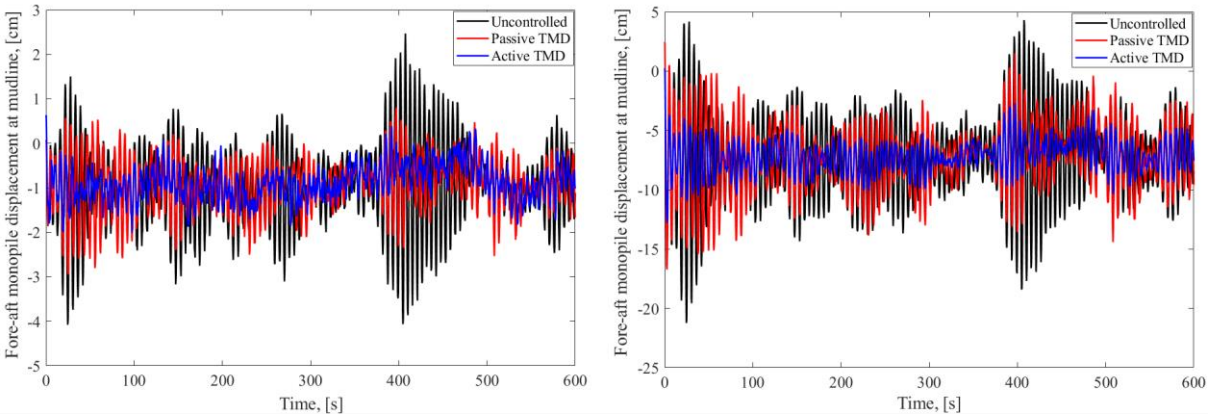

Figure 13: Fore-aft monopile displacement at mudline in [cm] with and without a TMD or ATMD for (a) LC6 and (b) LC10.

(a) Load case 6 (b) Load case 10

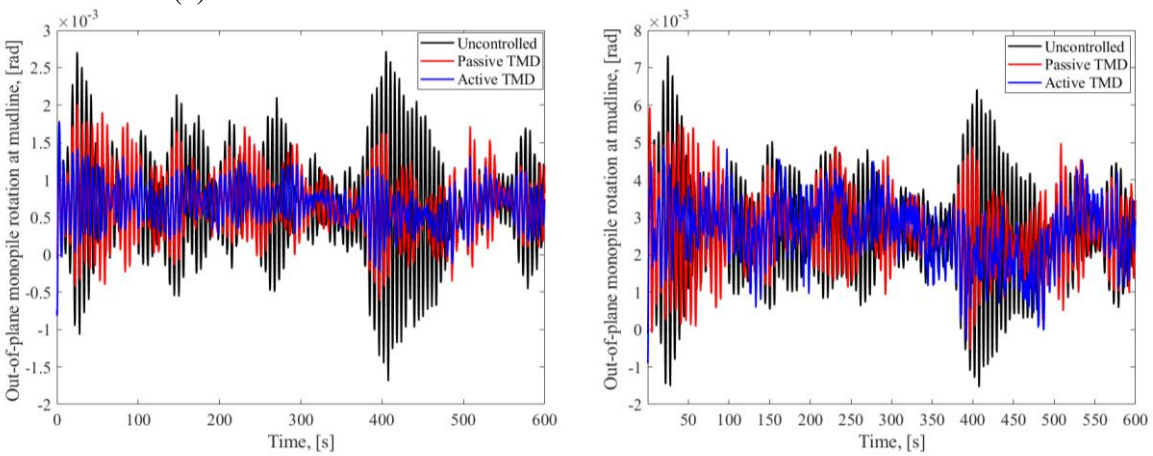

Figure 14: Monopile rotation time history with and without TMD or ATMD for (a) LC6 and (b) LC10.

To further analyze the effectiveness of the ATMD in the vibration reduction using the proposed combined FEA-active control scheme, three different TMD mass ratios were considered (i.e. 1%, 2% and 3%). Figures 15a and 15b illustrate respectively the comparison of the peak and RMS reduction values of the tower top fore-aft dispalcement as given by the passive TMD and the ATMD under LC10 and for the three different TMD mass ratios. It can be seen from Figures 15a and 15b that the reduction values of the passive and active TMD increase as the mass ratio increases from 1% to 3%. In this regard, the peak and RMS reduction values increase respectively from 28.5% and 38.9% (in the case of a passsive TMD with a mass ratio of 1%) to 37% and 52% (in the case of a passive TMD with a mass ratio of 3%). This corresponds to an

increase by around 30% for the peak vlaue and by 34% for the RMS; the reduction rate being lower in the case of the ATMD where an increase by around 26.6% and 9% for the peak and RMS values respectively was found as the ATMD mass ratio increases from 1% to 3%. Based on the results in Figure 15a and 15b, a mass ratio of 2% might be an appropriate option for the ATMD of the monopile-supported 10 MW OWT in terms of the peak and RMS reduction; the reduction being almost negligeable for a mass ratio beyond 2%.

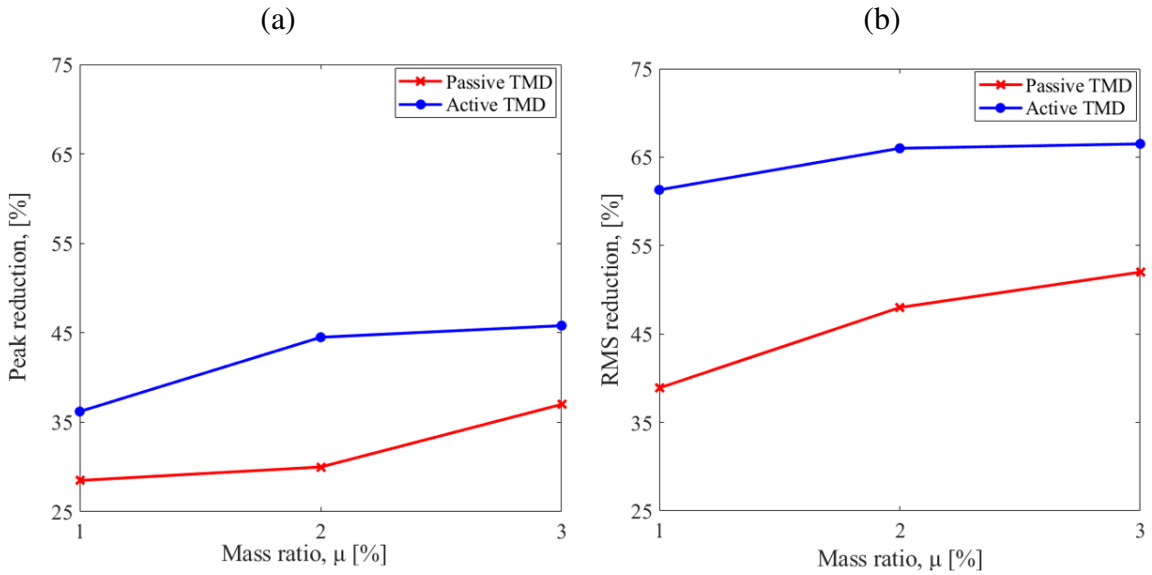

Figure 15: Reduction of the tower top fore-aft displacement under LC10 (a) peak reduction; (b) RMS reduction.

Another key parameter for the evaluation of the TMD and ATMD relevance of an OWT is the stroke which is the displacement of the TMD/ATMD mass inside the nacelle. The knowledge concerning the stroke is critical because of the limited space requirement inside the nacelle. Figure 16 compares the stroke between the passive TMD and the ATMD for LC6, LC10 and LC17 as obtained using the 3D mechanical model for a TMD with a 1% mass ratio. It is clear from Figure 16 that the ATMD stroke is quite important, and larger than what would actually be feasible in practice. Future work will incorporate stroke constraints within the 3D mechanical model and/or the control algorithm.

Figures 17 (a) and (b) compare the maximum and the RMS values of the stroke as given by the ATMD and the passive TMD for the three different TMD mass ratios (1%, 2% and 3%) under

LC10. From Figure 17, it was found that the maximum and RMS of the TMD and ATMD stroke decrease with the increase of the mass ratio where the maximum and RMS values of the TMD stroke decreases respectively by around 57% and 59% for the passive TMD and 24% and 25% for the ATMD as the mass ratio increases from 1% to 3%.

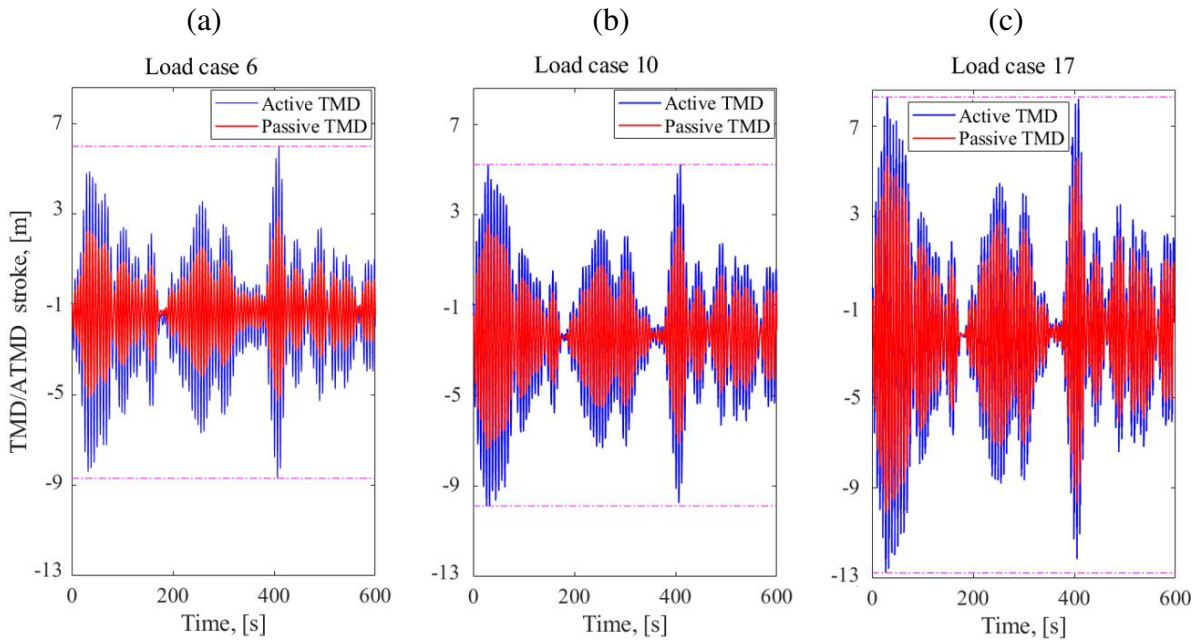

Figure 16: Stroke of the TMD and ATMD for (a) LC6, (b) LC10 and (c) LC17 for a TMD mass ratio of 1%.

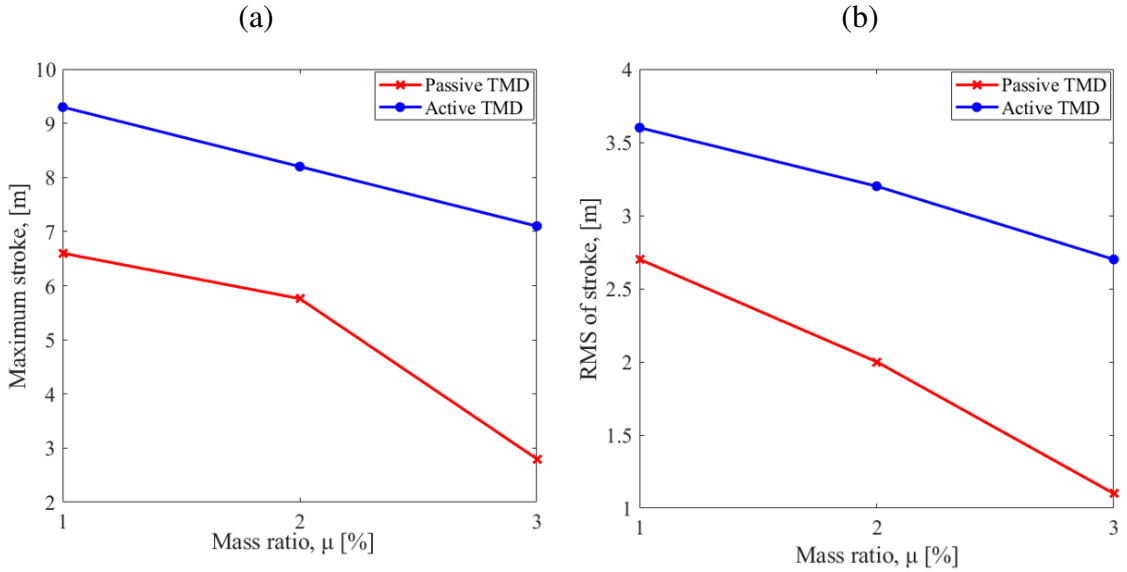

Figure 17: Passive TMD and ATMD stroke comparison under LC10 with different TMD mass ratios.

Finally, while the focus has been put on the vibration reduction on the tower top and on the foundation at mudline, it is worthwhile to discuss the cost of the active control system which is

measured using the active control power in kW. Figure 18 gives the active control power required to achieve the vibration mitigation for LC6, LC10 and LC17 using an ATMD having a mass ratio of 1%. The active control power was computed by multiplying the ATMD active control force (output of the controller) and the fore-aft velocity of the ATMD inside the nacelle. Based on Figure 18, the peak active control power requirement to achieve the vibration reduction is around 750 kW for LC6, 842 kW for LC10 and 1155 kW for LC17. These values correspond to 7.5% for LC6, 8.42% for LC10 and 11.55% for LC17 of the DTU rated power (10 MW).

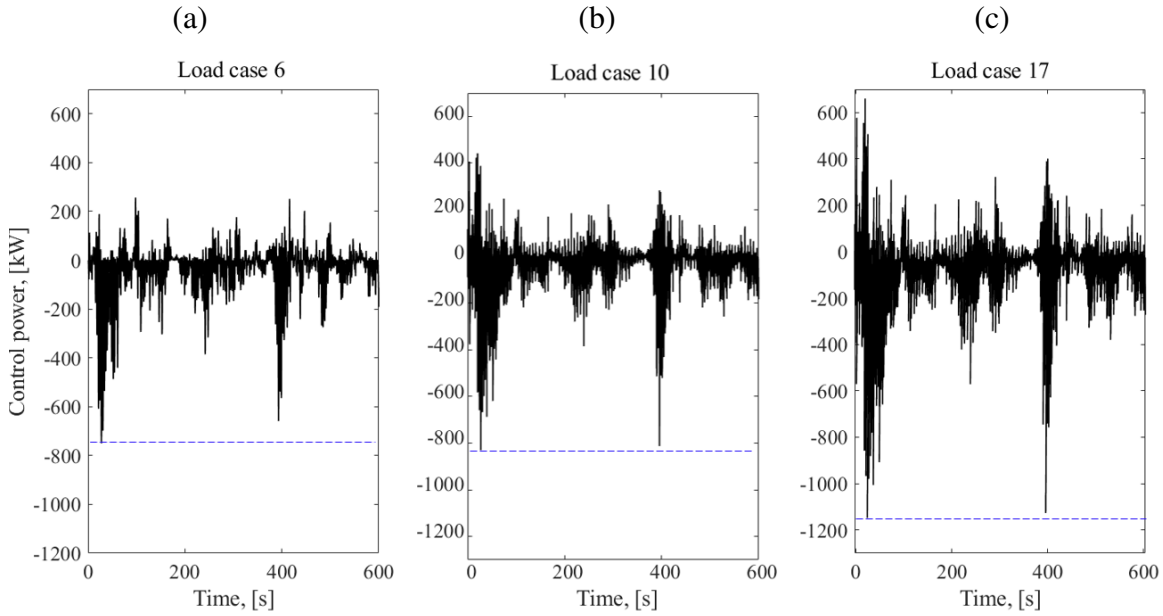

Figure 18: Control power time histories for (a) LC6, (b) LC10 and (c) LC17 using an ATMD with a 1% mass ratio.

When comparing the passive TMD and the active one (ATMD), the tradeoff is clear: active control resulted in increased vibration reduction (Figures 10-12) but at the expense of active power consumption and larger strokes (Figure 16). This is a balance that a designer must be aware of when deciding between the two approaches.

4.3 Relevance of the reduction of the MDOF model and the incorporation of a state-space observer within the active controller

In order to check the relevance of the proposed observer-based controller synthetized based on a fourth-order reduced MDOF analytical model, the performance of the ATMD as obtained using the controller synthesized from the fourth-order reduced MDOF model (i.e. with only 4 DOF, see section 3.2) was compared with that of the ATMD synthesized using the complete MDOF model (i.e. with all 11 DOF, see section 3.1). Figure 19 shows the results of this comparison for the three load cases LC6, LC10 and LC17. From this figure, it can be observed that the fourth-order MDOF model gives accurate results compared to the complete MDOF model where the RMS relative error was found to be lower than 0.2% for the three considered load cases. Based on the results shown in Figure 19, the significant reduction of the number of degrees of freedom of the MDOF model has proved to be efficient in terms of the reduction of the tower top fore-aft vibration for a monopile-supported OWT using an ATMD.

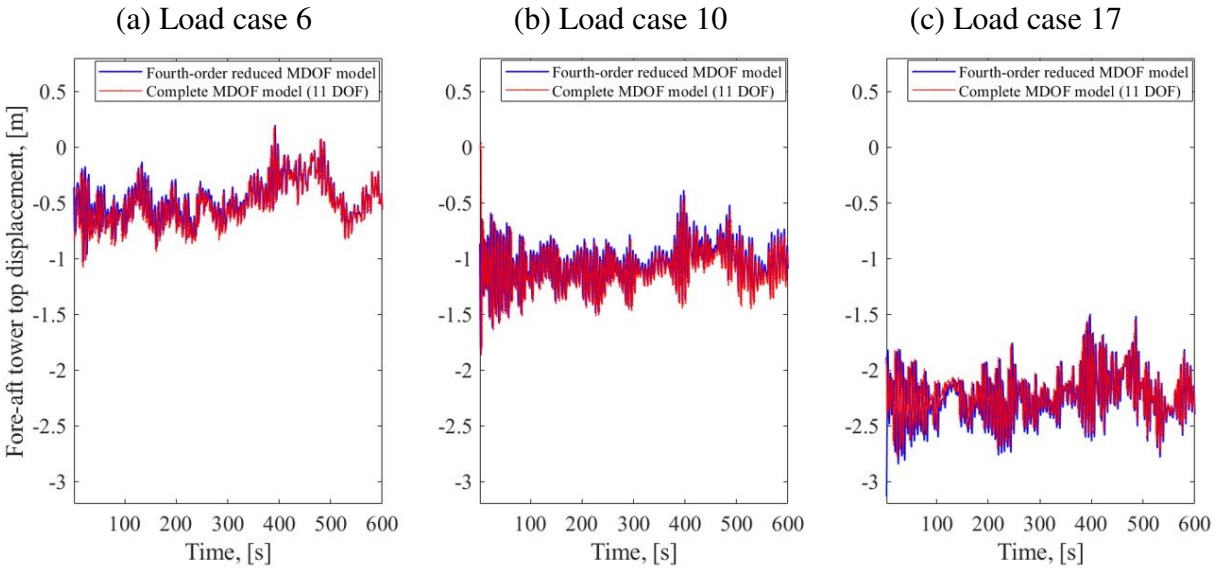

Figure 19: Comparison of the fore-aft tower top displacement in the case of an ATMD synthetized from the complete or reduced order MDOF model under (a) LC6, (b) LC10 and (c) LC17.

To check the relevance of the incorporation of a state observer (estimator) within the active controller to find all system states from the measurement of only one sensor output (i.e. the tower top fore-aft velocity), the performance of the ATMD as obtained using the controller

synthesized from the fourth-order reduced MDOF model (i.e. with only 4 DOF) combined with a state-space observer was compared with that of the ATMD synthesized using the same controller but in the absence of the state-space observer. Figure 20 shows the results of this comparison for two load cases LC10 and LC17. From this figure, it can be seen that the reduction of the required number of sensors *via* the incorporation of the observer gives accurate results compared to the controller without an observer (i.e. all the states of the OWT system are measured using sensors). The RMS relative error was found to be lower than 0.15% for the two considered load cases. Based on the results shown in Figure 20, the significant reduction of the required number of sensors by the implementation of a state observer within the active controller proved to be an efficient solution when designing an ATMD control system for the fore-aft vibration reduction of an OWT.

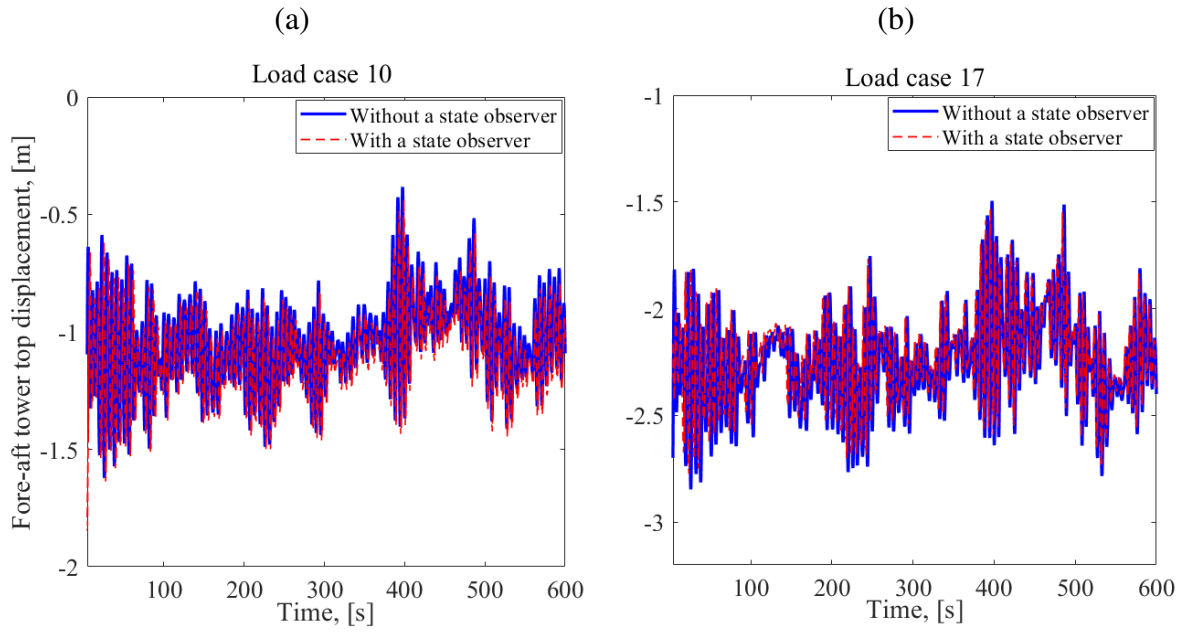

Figure 20: Comparison of the fore-aft tower top displacement in the case of an ATMD synthetized from the reduced-order MDOF model in the presence and absence of a state observer under (a) LC10 and (b) LC17.

5. Conclusions

Large deformation three-dimensional (3D) finite element (FE) analysis and observer-based active control were combined together in order to study the true real-time performance of an active tuned mass damper (ATMD) in reducing the tower fore-aft vibration of a monopile-supported multi-megawatt DTU 10 MW offshore wind turbine (OWT) subjected to stochastic wind and wave loads. Firstly, a 3D high-fidelity FE mechanical model of the OWT was developed using the standard FE code Abaqus. This model includes a TMD placed at the tower top. The developed structural model explicitly considers the real geometrical configuration of the OWT. It also considers a suitable monopile-soil interaction model, a realistic loading distribution along the OWT tower and blades and the large deformation of the OWT superstructure and monopile foundation. Indeed, the increasing capacity of next-generation OWTs renders their structure highly flexible and sensitive to dynamic loading, thus requiring a high-fidelity structural model that takes into account the structure large deformation and ensures an accurate prediction of their dynamic responses. Secondly, the developed 3D FE structural model was coupled with an optimal LQ active controller combined with a LQ state observer making use of a co-simulation technique. The aim of the observer is to reduce the number of required sensors as not all states can be measured in practice. The proposed observer-based LQ controller was synthetized using a reduced order linear time-invariant model derived from an existing coupled MDOF analytical model by Sun (2018). The aim of the reduction is to increase the effectiveness of the co-simulation technique.

10-minutes nonlinear implicit dynamic simulations were performed using Abaqus for two operational load cases (LC6 and LC10) and a standing still load case (LC17) to evaluate the performance of the ATMD based on the proposed co-simulation technique by comparing the

OWT dynamic responses in the presence of the ATMD control system with those (i) in the absence of a TMD and (ii) in the presence of a passive TMD.

From this paper, the following conclusions and practical guidance can be drawn:

* The technique of co-simulation presented in this paper can provide a valuable support to current design practice of OWTs in the presence of an active or even semi-active TMD particularly at the final design stage to accurately capture the OWT dynamic response making use of a high-fidelity large deformation FE model for the OWT. The proposed co-simulation technique offers also the advantage of being able to incorporate advanced soil constitutive models in the analysis where the soil behavior can be explicitly considered. Such advantage offered by the 3D high-fidelity FE model can provide insights about the performance of ATMDs in certain complex situations that an OWT can encounter during its lifetime such as soil liquefaction under earthquake loading or even under storm conditions and the long-term degradation of soil stiffness due to the stochastic/cyclic nature of wind and wave loads.
* The significant reduction of the required number of sensors by the implementation of a state observer within the active controller proved to be an efficient solution for practical applications when designing an ATMD control system for the fore-aft vibration reduction of monopile-supported OWTs. Indeed, the measurement of only the tower top fore-aft velocity was found to be sufficient to estimate all system states.
* The developed observer-based controller synthetized based on a reduced-order MDOF analytical model (with only 4 DOF) was found to be very efficient. In this regard, the proposed controller designed based on the reduced MDOF model was found to give very similar results compared to the one designed based on the complete MDOF model (with 11 DOF); the RMS deviation error of the tower top fore-aft displacement was found to be lower than 0.2%. Notice also that, the observer-based

controller developed from the reduced-order MDOF model was found to be remarkably capable of reducing the fore-aft RMS and peak displacements of (i) the tower top and (ii) the foundation at mudline, under load cases LC6, LC10 and LC17; the RMS reduction ratio of the tower top displacement with respect to the uncontrolled case (absence of a TMD) are around 59.2% for LC6, 61.3% for LC10 and 51% for LC17 and (ii) the peak reduction ratio being around 45.6% for LC6, 36.2% for LC10 and 29.1% for LC17 when the TMD mass ratio is 1%.

* The ATMD practical performance (in terms of the vibration reduction) evaluated based on the proposed co-simulation technique was found to be accompanied by important strokes inside the nacelle which were found as expected to decrease with the increase of the ATMD mass ratio, the relative peak reduction being around 24 % as the mass ratio increases from 1% to 3%. It should be noted that the ATMD important strokes inside the nacelle would actually be unfeasible in practice. In this regard, stroke limiters and/or nonlinear controllers are being anticipated for future work within the 3D high-fidelity FE model.

The Fortran subroutine as well as the 3D mechanical model used for the simulations presented herein can be obtained from the first author upon request.

Acknowledgments
This work is carried out within the framework of the WEAMEC, West Atlantic Marine Energy Community, and the funding from the CARENE, Communauté d'Agglomération de la Région Nazairienne et de l'Estuaire.

References

Aasen, S., Page, A.M., Skjolden Skau,, K., Anders Nygaard, T., 2017. Effect of foundation modelling on the fatigue lifetime of a monopile-based offshore wind turbine. *Wind Energy Sci.*;2:361–376. https://doi.org/10.5194/wes-2-361-2017

ABAQUS, 2013. Finite element analysis program. Version 6.13. Providence, USA

Alkhoury, P., Soubra, A.H., Rey, V., Aït-Ahmed, M., 2021. A full three-dimensional model for the estimation of the natural frequencies of an offshore wind turbine in sand. *Wind Energy*:1–21. https://doi.org/10.1002/we.2598.

Jonkman, B.J., Kilcher, L., 2012. TurbSim User's Guide: Version 1.06.00. National Renewable Energy Laboratory: Technical report.

Kwakernaak, H., Sivan, R., 1972. Linear Optimal Control Systems. *Journal of Dynamic Systems, Meausrement and Control*., https://doi.org/10.1115/1.3426828

Lackner, M.A., Rotea, M.A., 2011a. Passive structural control of offshore wind turbines. *Wind Energy*; 1–20. https://doi.org/10.1002/we

Lackner, M.A., Rotea, M.A., 2011b. Structural control of floating wind turbines. *Mechatronics*; 21:704–719. https://doi.org/10.1016/j.mechatronics.2010.11.007

LeBlanc, C., 2009. Design of offshore wind turbine support structure structures, [Ph.D. Thesis], Aalborg University of Denmark.

Murtagh, P.J., Ghosh, A., Basu, B., Broderick, B.M., 2008. Passive control of wind turbine vibrations including blade/tower interaction and rotationally sampled turbulence. *Wind Energy*; 11: 305–317. https://doi.org/10.1002/we.249

Nagarajaiah, S., 2009. Adaptive passive, semiactive, smart tuned mass dampers: identification and control using emperical mode decomposition, hilbert transform, and short-term fourier transform. *Struct. Control Heal. Monit.*;16:800-841. https://doi.org/10.1002/stc.349

Oveisi, A., Sukhairi, T.A., Nestorović, T., 2018. Finite element-based software-in-the-loop for offline post-processing and real-time simulations. *Struct. Eng. Mech.*;67:643–658. https://doi.org/10.12989/sem.2018.67.6.643

Rahman, M., Ong, Z.C., Chong, W.T., Julai, S., Khoo, S.Y., 2015. Performance enhancement of wind turbine systems with vibration control: A review. *Renew. Sustain. Energy Rev.*;51:43–54. https://doi.org/10.1016/j.rser.2015.05.078

Ray, L.R., Koh, B-H., Tian, L., 2000. Damage detection and vibration control in smart plates: Towards multifunctional smart structures. *J. Intell. Mater. Syst. Struct.*;11: 725-739. https://doi.org/10.1106/7DK5-6R4Q-H727-P5T7

Shinozuka, M., 1972. Monte Carlo solution of structural dynamics. *Comput. Struct.*;2 :855–874. https://doi.org/10.1016/0045-7949(72)90043-0

Smith, M., 2015. ABAQUS documentation collection. Simulia.

Sonmez, E., Nagarajaiah, S., Sun, C., Basu, B., 2016. A study on semi-active Tuned Liquid Column Dampers (sTLCDs) for structural response reduction under random excitations. *J. Sound Vib.*;362:1–15. https://doi.org/10.1016/j.jsv.2015.09.020

Sun, C., 2018. Semi-active control of monopile offshore wind turbines under multi-hazards. *Mech Syst Signal Pr.*; 285–305. https://doi.org/10.1016/j.ymssp.2017.06.016

Sun, C., Jahangiri, V., 2018. Bi-directional vibration control of offshore wind turbines using a

3D pendulum tuned mass damper. *Mech. Syst. Signal Process.*;105:338–360. https://doi.org/10.1016/j.ymssp.2017.12.011

Sun, C., Nagarajaiah, S., 2014. Study on semi-active tuned mass damper with variable damping and stifffness under seismic excitations. *Struct. Control Heal. Monit.*;21:890-906. https://doi.org/10.1002/stc.1620

Sun, C., Jahangiri, V., Sun, H., 2021. Adaptive bidirectional dynamic response control of offshore wind turbines with time-varying structural properties. *Struct. Control Heal. Monit*. https://doi.org/10.1002/stc.2817

Veers, P., 1988. Three-dimensional wind simulation, SAND88-0152, UC-261, Sandia National Laboratories, Albuquerque, NM.

von Wolffersdorff, P.A., 1996. Hypoplastic relation for granular materials with a predefined limit state surface. *Mech. Cohesive-Frictional Mater.*;1:251–271. https://doi.org/10.1002/(SICI)1099-1484(199607)1:3<251::AID-CFM13>3.0.CO;2-3

Zhang, Z., Hoeg, C., 2021. Inerter-enhanced tuned mass damper for vibration damping of floating offshore wind turbines. *Ocean Engineering*.;223. https://doi.org/10.1016/j.oceaneng.2021.108663

Zhu, B., Sun, C., Jahangiri, V., 2021. Characterizing and mitigating ice-induced vibration of monopile offshore wind turbines. *Ocean Eng.*;219:108406. https://doi.org/10.1016/j.oceaneng.2020.108406

Zuo, H., Bi, K., Hao, H., 2017. Using multiple tuned mass dampers to control offshore wind turbine vibrations under multiple hazards. *Eng. Struct.*; 141: 303–315. https://doi.org/10.1016/j.engstruct.2017.03.006

Zuo, H., Bi, K., Hao, H., 2018. Dynamic analyses of operating offshore wind turbines including soil-structure interaction. *Eng. Struct*;157:42–62.

Zuo, H., Bi, K., Hao, H., 2020. A state-of-the-art review on the vibration mitigation of wind turbines. *Renew Sustain Energy Rev.*; (121) 109710. https://doi.org/10.1016/j.rser.2020.109710